Instituto Nacional de Astrofísica,
Óptica y Electrónica.

Towards a Single Photon Frequency Conversion

Por:
Oscar Adrián Jiménez Gordillo

Tesis sometida como requisito parcial para obtener el grado de
Maestro en Ciencias en la Especialidad de Óptica
En el Instituto Nacional de Astrofísica, Óptica y Electrónica

Supervisada por:
Dr. Antonio Badolato
Dr. José Javier Sánchez Mondragón
Dr. Jorge Roberto Zurita Sánchez

Fecha de examen profesional	29 de mayo del 2015
Director Externo	Dr. Antonio Badolato
Director Interno	Dr. José Javier Sánchez Mondragón
Co-director	Dr. Jorge Roberto Zurita Sánchez
Jurado de examen profesional	Dr. José Francisco Renero Carrillo
	Dr. José Amparo Andrade Lucio
	Dr. J. Jesús Escobedo Alatorre

A mis padres

Abstract

Quantum frequency up-conversion (QFC) of non-classical states of light allows the integration of different quantum systems working at different energies. This process takes advantage of telecommunication wavelengths photons for optical fiber transmission of quantum information, and near visible wavelengths for data manipulation and storage. The key objective of QFC is to guarantee that the input photon number probability distribution is maintained after the conversion process. With this, we will be able to efficiently study the single-photon emission properties of epitaxial InAs/GaAs quantum dots embedded in a photonic crystal nanocavities without the problems that inefficient IR wavelengths detectors imply. The up-conversion process consists on combining two optical fields, in a nonlinear medium, to generate a third field that is equal to the two inputs frequency sum. To fulfill the momentum conservation, required by this process, we need to compensate the wave vector mismatch between the output and input beams. This is achieved by using a grating in the nonlinear medium, a process named quasi-phase matching (QPM). In this work we use a Zinc doped periodically poled $LiNbO_3$ (Zn:PPLN WG) waveguide as the nonlinear material. To achieve the quantum frequency conversion of a semiconductor quantum dot (QD) single photons emission, embedded in a photonic crystal nanocavity, we started by characterizing the performance of the PPLN-WG in the optical power macro-regime. Signal photons, produced by an 1175nm laser, simulating our QD emission line, are combined with pump photons, produced by a C-band laser, with a dichroic mirror before entering the PPLN waveguide. In order to achieve the phase matched wavelength in the PPLN, its temperature must be finely tuned. The signal coming out of the PPLN waveguide is filtered and analyzed.

Resumen

La conversión cuántica de frecuencia (QFC) de estados de luz no clásicos permite la integración de diferentes sistemas cuánticos trabajando a diferentes energías. Este proceso toma ventaja de los fotones en la banda de telecomunicaciones para transmitir información cuántica a través de fibras ópticas y de los fotones en el visible para

manipular y almacenar la información. El objetivo principal de la QFC es garantizar que la distribución de probabilidad de los fotones de entrada se mantenga después del proceso de conversión. Con esto, será posible estudiar eficientemente la propiedad de emisión de fotones individuales de puntos cuánticos epitaxiales de InAs/GaAs embebidos en nanocavidades de cristales fotónicos sin tener los problemas de detección que presentan los detectores de avalancha en el infrarrojo. El proceso de conversión consiste en combinar dos campos ópticos en un medio no lineal para generar un tercer campo con una frecuencia igual a la suma de la de los campos de entrada. Para lograr la conservación de momento requerida por este proceso, se necesita compensar la el desfase entre vectores de onda de los campos de entrada y salida. Esto se logra usando una rejilla en el medio no lineal, este proceso se llama quasi-phase matching (QPM). En este trabajo usamos una guía de onda de $LiNbO_3$ dopada con Zinc polarizada periódicamente (Zn:PPLN WG) como el material no lineal. Para lograr la QFC de la emisión de puntos cuánticos comenzamos por caracterizar el rendimiento de la PPLN-WG con potencias de luz en el macro régimen. Fotones de señal, producidos por un láser a 1175nm que simulan la línea de emisión de los puntos cuánticos, son combinados con fotones de bombeo producidos por un láser a 1550nm mediante un espejo dicroico antes de hacerlos incidir en la PPLN-WG.

Contents

1. Introduction

Since the conception of the quantum key distribution (QKD) by Bennet & Brassard in 1984 (Bennet & Brassard, 1984), we have realized that quantum networks provide opportunities and challenges across a range of intellectual and technical frontiers, including quantum computation, communication and metrology (Zoller, et al., 2005). To achieve quantum networks composed of many elements and channels, we require new scientific capabilities for generating and characterizing quantum coherence and entanglement. A fundamental piece to this endeavor are quantum interfaces, which convert quantum states from one physical system to those of another in a reversible manner, this is where our work is situated. Such quantum connectivity in networks can be achieved by the optical interactions of single photons and atoms, allowing the distribution of entanglement across the network and the teleportation of quantum states between the different elements and devices (Kimble, 2008). The preeminent obstacle to the development of quantum information technology is the difficulty of transmitting quantum information over noisy and lossy quantum communication channels, recovering and refreshing the quantum information that is received and then storing it in a reliable quantum memory (Shapiro, 2002).

The objective of quantum information processing (QIP) is to use quantum superposition states to transmit, store, and process information. In classical communication, information is transferred and encoded in pulses of light. The pulses are detected by photodetectors, transformed into electrical current pulses, amplified by electronics, and sent to computers, phones, etc. This transformation of light into electrical signals forms a classical light-matter interface. In QIP simple classical detection of light is inadequate for recording into memory, because it destroys the quantum state by adding extra noise to it. Instead of direct transformation of light pulses into electrical pulses, as in classical communication, quantum state transfer of qubits has to be developed in QIP (Zoller, et al., 2005). The additional structure in the qubit leads to extraordinary computational and communications abilities that do not exist with

classical hardware. It is unlikely that future quantum information processors and communication systems will be composed of units based on a single type of physical system such as a particular kind of atomic ensemble, trapped ion, semiconductor, or superconductor. Instead, hybrid networks are expected to emerge, in which different types of physical systems play different roles (O'Brien, Furusawa, & Vučković, 2009). These systems will include computational nodes containing atoms or superconductors, for example that act as quantum memories or processors. To communicate quantum information, each node will absorb and emit photons at its own natural resonance frequency and line shape. This diversity of possible nodes creates a challenge: how to convert a single photon from one frequency to another and alter its wavepacket shape to fit optimally with different systems. In other words, it is like if two types of quantum nodes were speaking a different language and a translating device was needed to get the message from one to the other. Hence a quantum interface has to be developed. Figure 1-1 illustrates this notion of interface (Raymer & Srinivasan, 2012).

In conclusion, an interface between quantum information carriers (quantum states of light) and quantum information storage and processors (atoms, ions, solid state) is an integral part of a full-scale quantum information system. It is obvious that long lived entanglement shared over a long distance requires transfer of entanglement from light (the long distance carrier) to atoms (the long lived objects). Such transfer can only be done via a special light-atoms quantum interface. The eventual goal is to spread quantum-state entanglement throughout a large network of memories or processors**.** (Zoller, et al., 2005).

1.1 Quantum communications

Quantum communication is the art of transferring a quantum state from one place to another. The basic motivation is that quantum states code quantum information, called qubits, and that quantum information allows tasks to be performed far much efficiently than using classical information. The field of quantum communication has established itself over recent years due to its driving force, QKD, and to the fascinating process of quantum teleportation. It will be an important part of

physics in the decades to come, with great challenges in quantum memories and repeaters for worldwide applications (Gisin & Thew, 2007).

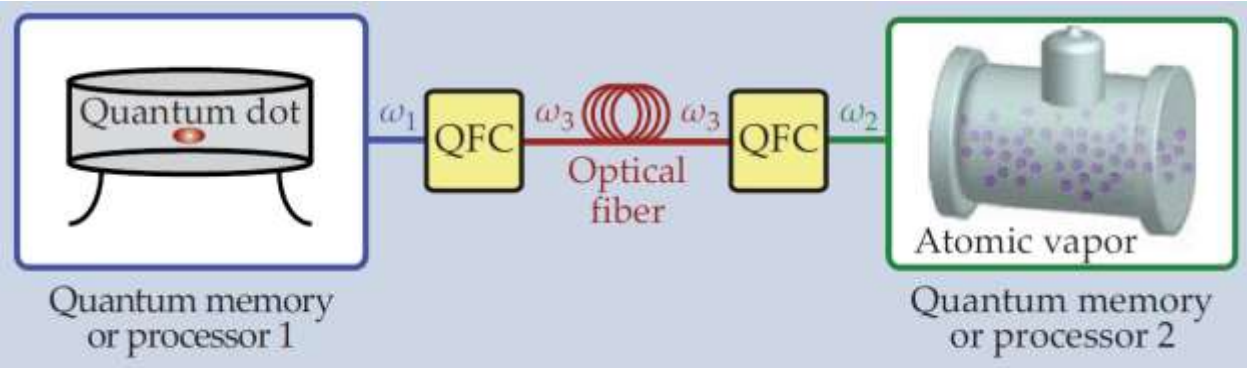

Figure 1-1. Future quantum information communication system. In it, a pair of quantum frequency conversion (QFC) devices connect a quantum dot operating at photon frequency ω_1 to an atomic vapor operating at frequency ω_2 through an optical fiber that optimally transmits light at frequency ω_3. After Raymer & Srinivasan (2012).

As described in the previous paragraph, quantum communication requires the transfer of quantum states (Tittel & Weihs, 2001), or quantum bits of information (qubits), from one place to another. Fundamentally, this allows the distribution of entanglement and the demonstration of quantum non-locality over significant distances (Resch, et al., 2005). Within the context of applications, quantum cryptography offers a provably secure way to establish a confidential key between distant partners. Photons represent the natural flying qubit carriers for quantum communication, and the presence of telecommunications optical fibres makes the wavelengths of 1,310 nm and 1,550 nm particularly suitable for distribution over long distances. However, qubits encoded into alkaline atoms that absorb and emit at wavelengths around 800nm have been considered for the storage and processing of quantum information (Blinov, Moehring, Duan, & Monroe, 2004). Also in recent years, antibunched streams of photons produced by semiconductor quantum dots (QD) embedded in photonic crystal nanocavities have been observed, showing that quantum information tasks are achievable in solid-state cavity QED (Hennessy, et al., 2007). Hence, future quantum information networks made of telecommunications channels and different types of nodes will require interfaces that enable qubit transfers between these useful wavelengths, while preserving quantum coherence and entanglement. Superposition of quantum states and entanglement are the fundamental resources of quantum communication and quantum information

processing (Tittel & Weihs, 2001). The most appropriate carrier for QIP and associated encoding observable depend on the specific task. Photons have been proved suitable to transmit quantum information, and atoms or ions to store and process it. Depending on the quantum communication channel, the wavelength of the photonic carrier is also important. The use of telecommunications wavelengths (1,310 and 1,550 nm) is particularly advantageous when employing optical fibers, while free space transmission is mostly based on shorter wavelengths. Future realizations of quantum networks, containing elementary quantum processors and memories, connected by communication channels, require quantum interfaces capable of transferring qubit states from one type of carrier to another. This demands the reversible mapping between photons and atoms, which also includes the mapping between photons of different wavelengths. However, as opposed to the reproduction of classical information between different media, it is not possible to merely measure the properties of a given quantum system and replicate them accordingly, as a result of the no-cloning theorem (Wootters & Zurek, 1982). Nevertheless, it is possible to resort to a transfer of the quantum information based on an interaction that maintains the coherence properties of the initial quantum system. (Tanzilli, et al., 2005)

1.2 Quantum frequency conversion

One of the solution for the identified quantum interface problem of the previous paragraphs is the Quantum Frequency Conversion (QFC) experimental scheme, proposed by Kumar in 1990 (Kumar, 1990), in which the quantum states of two light beams of different frequencies can be interchanged. In his seminal paper Kumar shows that, in effect, it is possible to change the frequency of an input light beam while maintaining its quantum state. This scheme is based on the three-wave mixing processes that happen in materials with optical nonlinearities. Most phenomena in nonlinear optics are based on parametric oscillations, which occur in any oscillatory system whose parameters vary periodically in time. The parameter to be varied is typically the medium's electric susceptibility, the proportionality factor relating a driving field at a specific frequency to the induced electric dipole density. If strong light fields cause the dipoles to oscillate, then energy can be redistributed between optical modes of various frequencies. The dominant effect in this process is usually governed by the

second-order susceptibility χ(2) in noncentrosymmetric (lacking a center of symmetry) media such as lithium niobate or gallium arsenide crystals. Weak light of a given frequency ω_1 can be converted to ω_2 using the second-order nonlinear optical response. In this case a strong laser field—the pump—modulates the medium's susceptibility at frequency ω_p, which leads to light generation at the sum and difference frequencies $\omega_2 = \omega_1 \pm \omega_p$. A frequency increase is called up-conversion; a decrease, down-conversion. Quantum frequency conversion (QFC), is the process of changing the frequency of a quantum state of light—for example, a single-photon state—without changing its other state properties in an uncontrolled way. Of particular importance is that photon momentum must be conserved in the course of QFC, or, in the jargon of the field, phase matching must be ensured. (Raymer & Srinivasan, 2012). Figure 1-2 shows an example of a device that enables an increase in the frequency of a single photon (up-conversion) as we will see in Section 2.1.4.

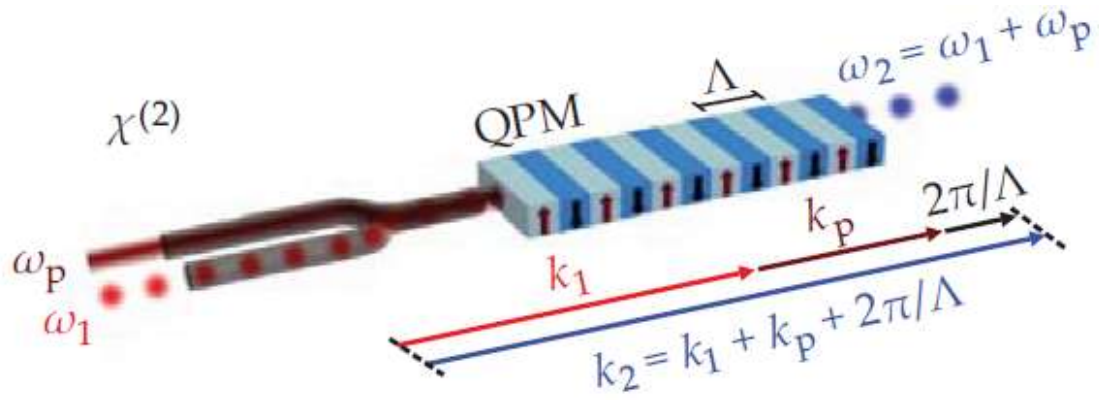

Figure 1-2. Schematic diagram of QFC by means of Quasi-phase matching in an optically nonlinear material. The up-conversion is governed by the second-order susceptibility $\chi^{(2)}$ of the material. A strong pump laser at frequency ω_p, converts input photon pulses at $\omega 1$ to output pulses at $\omega_2 = \omega_1 + \omega_p$. A uniform material would not satisfy phase matching, because $k_2 \neq k_1 + k_p$. Thus the illustrated device uses quasi-phase matching (QPM); as shown below the device in the panel, a spatially periodic change (with period Λ) in the material properties of the nonlinear medium compensates for the momentum mismatch, after (Raymer & Srinivasan, 2012).

In the other hand, single-photon detection at wavelengths in the fiber-optic communications band is important for quantum-optics applications, such as quantum cryptography (Bourennane, Karlsson, Pena Ciscar, & Mathés, 2001). High detection efficiency near 1.55 μm permits compatibility with existing fiber-optics technology in which fiber losses are minimized. Current detection devices operating at these wavelengths cannot deliver the performance needed to implement, for example, QKD

over distances longer than a few tens of kilometers because of limitations imposed by high dark counts and low detection efficiencies in two of the more prominent devices currently used, which are InGaAs–InP avalanche photodiodes (APDs) and solid-state photomultipliers (Bourennane, et al., 1999). In contrast, single-photon detection in the near-infrared (NIR; 600–800 nm) can be performed efficiently with silicon APDs. One can take advantage of these detectors if efficient conversion from 1.55 mm to the NIR is available. Frequency upconversion of weak signals is possible by sum-frequency generation (SFG) with a stronger pump wave as described in the previous paragraph. Single-photon detection of 1.55-mm photons by means of frequency upconversion in a waveguide of periodically poled lithium niobate (PPLN) was recently demonstrated. It offers the convenience of nonresonant single-pass operation and moderate pump power requirement. For efficient conversion in nonlinear optical frequency mixing, high field intensities and long interaction lengths are necessary, both of which can be achieved simultaneously in a guided-wave structure (Roussev, Langrock, Kurz, & Fejer, 2004).

1.3 Objectives and outline of this thesis

The main objective of this thesis is to up-convert single photons emitting at a wavelength of 1180nm produced by a quantum dot (QD) embedded in photonic crystal (PC) nanocavity to a wavelength of 670nm in the visible range. We want to achieve this quantum frequency up-conversion to characterize our single photon source with Silicon single-photon detectors in the visible that perform better than infrared single photon detectors. Moreover we want to overcome spectral distinguishability common to inhomogeneously broadened solid-state quantum emitters by converting spectrally separated QD transition to the same wavelength. To achieve our objective, we can divide the work in three stages:

1) Characterization of the periodically poled lithium niobate waveguide (PPLN-WG) nonlinear device in the macro-regime.
2) Demonstrate and characterize the quantum frequency up-conversion of attenuated laser pulses, simulating a single photon source.

3) Demonstrate and characterize the quantum frequency up-conversion of single photons emitted from a QD in a PC nanocavity.

It is worth reminding that, due to the time limitations of a M.Sc. project, the experiments done in this thesis only cover the first stage of the whole project, the characterization of the PPLN-WG.

We will begin in Chapter 2 by explaining the theoretical nonlinear and quantum optics foundations for this work. Then in Chapter 3 I proceed to describe the optical properties of our PPLN-WG device. Finally, in Chapter 4 every aspect of the experiment is detailed and the obtained results are explained.

2. Theoretical Background

In this chapter we describe the theoretical foundations to understand the experiments done in this work. Because this work lies in the border of nonlinear and quantum optics we need to know some concepts about both fields. Section 2.1 explains the process of frequency conversion and the techniques to achieve it. Section 2.2 presents an introduction to the quantum description of light, needed to explain the frequency conversion of quantum states of light.

2.1 Nonlinear Optics

Nonlinear optics is the study of phenomena that occur when the presence of light in a material modifies its optical properties. This modification is typically achieved with laser light. These phenomena are “nonlinear” because they occur when the response of a material to an applied optical field depends in a nonlinear manner on the strength of the optical field. For our work, the nonlinear material is the lithium niobate.

In order to describe precisely what an optical nonlinearity means we will first consider how the dipole moment per unit volume, or polarization *P*(t), of a material depends on the strength of an applied optical field *E*(t).The reason why the polarization plays a key role in the description of nonlinear optical phenomena is that a time-varying polarization can act as the source of new components of the electromagnetic field. For this section we follow the treatment given by (Boyd, 2007).

2.1.1 Nonlinear Polarization

When an external electric field ***E*** is applied to a dielectric medium a polarization ***P*** is induced. In the case of linear optics, the induced polarization can be often described by the relationship

$$P_i = \epsilon_0\left[\chi_{ij}^{(1)}E_j + \chi_{ijk}^{(2)}E_jE_k + \chi_{ijkl}^{(3)}E_jE_kE_l + \cdots\right], \tag{2.1.1}$$

where the $\chi^{(n)}$ are tensors of rank n+1 known as the nth-order susceptibilities and ϵ_0 is the permittivity of free space. When electric fields and/or higher-order susceptibilities become large, the nonlinear terms $P_i^{(NL)} = P_i^{(2)} + P_i^{(3)} + \ldots$ come into play. Then, nonlinear optical effects can be observed. Physical processes that occur as a result of the second-order polarization $\boldsymbol{P}^{(2)}$ tend to be distinct from those that occur as a result of the third-order polarization $\boldsymbol{P}^{(3)}$. The first two polarization terms read:

$$P_i^{(1)} = \epsilon_0 \sum_{jk} \sum_n \chi_{ij}^{(1)}(\omega_n)\, E_j(\omega_n) e^{-i\omega_n t}, \tag{2.1.2}$$

$$P_i^{(2)} = \epsilon_0 \sum_{jk} \sum_{(nm)} \chi_{ijk}^{(2)}(\omega_n + \omega_m\,;\omega_n, \omega_m)\, E_j(\omega_n) E_k(\omega_m) e^{-i(\omega_n+\omega_m)t}. \tag{2.1.3}$$

There a number of nonlinear optical processes that can occur. In this thesis we will focus particularly in second-order nonlinear effects. From Eq. (2.1.3) we can see that the second-order nonlinear polarization is responsible for three-wave mixing processes, this is the circumstance in which the optical field incident upon a second-order nonlinear medium consists of two distinct frequency components, which we represent in the form

$$\boldsymbol{E}(t) = \mathbf{E}_1 e^{-i\omega_1 t} + \mathbf{E}_2 e^{-i\omega_2 t} + \text{c. c.} \tag{2.1.4}$$

Then, plugging (2.1.4) into (2.1.3) we find that the nonlinear polarization is given by

$$\boldsymbol{P}^{(2)} = \epsilon_0 \chi_{ijk}^{(2)} \left[\mathbf{E}_1^2 e^{-2i\omega_1 t} + \mathbf{E}_2^2 e^{-2i\omega_2 t} + 2\mathbf{E}_1\mathbf{E}_2 e^{-i(\omega_1+\omega_2)t} + 2\mathbf{E}_1\mathbf{E}_2^* e^{-i(\omega_1-\omega_2)t} + \text{c. c.}\right] + 2\epsilon_0 \chi_{ijk}^{(2)} [\mathbf{E}_1\mathbf{E}_1^* + \mathbf{E}_2\mathbf{E}_2^*]. \tag{2.1.5}$$

We now see that in Eq. (2.1.5) we have the terms

$\epsilon_0 \chi^{(2)} \mathbf{E}_1^2 e^{-2i\omega_1 t} + c.c$	second harmonic generation (**SHG**) of ω_1,	
$\epsilon_0 \chi^{(2)} \mathbf{E}_2^2 e^{-2i\omega_2 t} + c.c$	second harmonic generation (**SHG**) of ω_2,	
$2\epsilon_0 \chi^{(2)} \mathbf{E}_1\mathbf{E}_2 e^{-i(\omega_1+\omega_2)t} + c.c.$	sum frequency generation (**SFG**),	(2.1.6)
$2\epsilon_0 \chi^{(2)} \mathbf{E}_1\mathbf{E}_2^* e^{-i(\omega_1-\omega_2)t} + c.c.$	difference frequency generation (**DFG**), and	
$2\epsilon_0 \chi^{(2)} [\mathbf{E}_1\mathbf{E}_1^* + \mathbf{E}_2\mathbf{E}_2^*] e^0$	optical rectification (**OR**).	

Here we have labeled each term by the name of the physical process it describes. We see from (2.1.6) that four different nonzero frequency components are present in the nonlinear polarization. The nonlinear polarization can efficiently produce an output signal only if a certain phase-matching condition (discussed in Section 2.1.3) is satisfied, and usually this condition cannot be satisfied for more than one frequency component of the nonlinear polarization. That is why no more than one of the frequency components in (2.1.5) will be present with any appreciable intensity in the radiation generated by the nonlinear optical interaction. In this work we are interested in the process of sum frequency generation, **SFG**.

The process of **SFG** is depicted in Figure 2-1 where in part (a) the input fields are at frequencies $\omega_1$and ω_2. Due to the nonlinearities in the atomic response of the material, each atom develops an oscillating dipole moment which contains a component at frequency $\omega_1 + \omega_2$. A single atom would radiate at this frequency in the form of a dipole radiation patter as shown in (b). However, any material sample contains an enormous number of atomic dipoles, each of them oscillates with a phase determined by the phase of the incident fields. If the relative phasing of these dipoles is correct, the field radiated by each dipole will add constructively in the forward direction as illustrated in part (c).

For the most general case, the second-order nonlinear susceptibilities $\chi_{ijk}^{(2)}(\omega_n + \omega_m\,;\omega_n, \omega_m)$ depend on three frequencies. But now, for simplicity we will assume that they are frequency independent. Instead of the second order nonlinear susceptibility, it is common to use the nonlinear coefficient $\mathbf{d} \equiv d_{ijk}$ given by the relation $d_{ijk} = \chi_{ijk}^{(2)}/2$.

2.1.2 Coupled-Wave Equations for Sum-Frequency Generation

To begin let us assume the configuration shown in Figure 2-2, where the applied waves fall onto the nonlinear medium at normal incidence. We consider the wave equation for an optically nonlinear, isotropic, lossless, and dispersive material

$$\nabla^2 \boldsymbol{E}_n - \frac{\epsilon^{(1)}(\omega_n)}{c^2}\frac{\partial^2 \boldsymbol{E}_n}{\partial t^2} = \frac{1}{\epsilon_0 c^2}\frac{\partial^2 \boldsymbol{P}_n^{NL}}{\partial t^2} \qquad (2.1.7)$$

Where $\epsilon^{(1)}$ is the real, frequency-dependent dielectric tensor. This wave equation can be used to describe specific nonlinear interactions and must hold for each frequency component of the field. We propose the solution to this equation as a plane wave at frequency ω_3 propagating in the +z direction in the form

$$\tilde{E}_3(z,t) = E_3 e^{-i\omega_3 t} + \text{c. c.} = A_3 e^{ik_3 z} e^{-i\omega_3 t} + \text{c. c.}, \qquad (2.1.8)$$

where

$$k_3 = \frac{n_3 \omega_3}{c}, \qquad n_3^2 = \epsilon^{(1)}(\omega_3). \qquad (2.1.9)$$

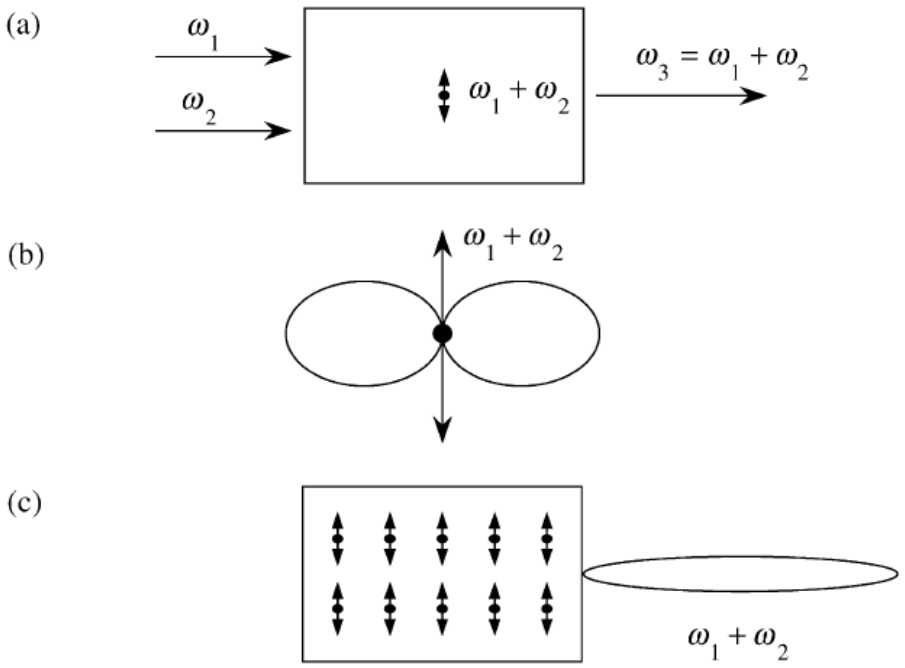

Figure 2-1. Sum-frequency generation process. After (Boyd, 2007).

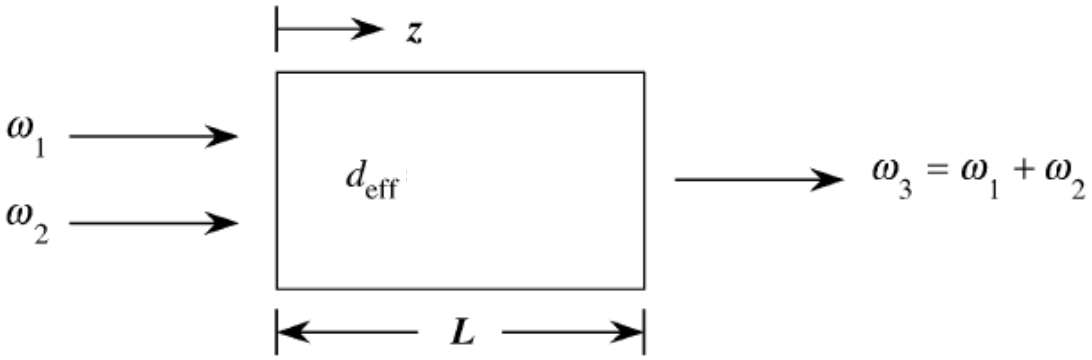

Figure 2-2 Sum-frequency generation configuration. After (Boyd, 2007).

We expect that the solution of (2.1.7) will be of the form of (2.1.8) with A_i taken to be a function of *z*. The nonlinear source term appearing in Eq. (2.1.7) is represented as

$$\tilde{P}_3(z,t) = P_3 e^{-i\omega_3 t} + \text{c.c} = 4\epsilon_0 d_{\text{eff}} E_1 E_2 e^{-i\omega_3 t} + \text{c.c} = 4\epsilon_0 d_{\text{eff}} A_1 A_2 e^{i(k_1+k_2)z} e^{-i\omega_3 t} + \text{c.c.} \quad (2.1.10)$$

where d_{eff} can be calculated from the **d** tensor if the propagation and polarization directions of all three fields are known and the Kleinman's symmetry condition is valid.

Now, we plug Eqs. (2.1.8) and (2.1.10) into the wave equation (2.1.7). After doing some calculation and taking into account the slowly varying amplitude approximation, we obtain the coupled-amplitude equation

$$\frac{dA_3}{dz} = \frac{2id_{\text{eff}}\omega_3^2}{k_3 c^2} A_1 A_2 e^{i\Delta kz} \quad (2.1.11)$$

where we have introduced the quantity

$$\Delta k = k_1 + k_2 - k_3, \quad (2.1.12)$$

which is called the wavevector (or momentum) mismatch. Equation (2.1.11) shows how the amplitude of the $\omega_3$wave varies as a consequence of its coupling to the ω_1 and ω_2 waves. We must also take into consideration the spatial variation of the ω_1 and $\omega_2$fields, so we can find two additional coupled-amplitude equations for them by repeating the derivation given above for ω_3.

$$\frac{dA_1}{dz} = \frac{2id_{\text{eff}}\omega_1^2}{k_1c^2} A_3 A_2^* e^{-i\Delta kz}, \quad (2.1.13)$$

$$\frac{dA_2}{dz} = \frac{2id_{\text{eff}}\omega_2^2}{k_2c^2} A_3 A_1^* e^{-i\Delta kz}. \quad (2.1.14)$$

2.1.3 Phase-matching

From Eq. (2.1.11) and by assuming that the amplitudes $A_1$and A_2 are constants, we note that, for the special case

$$\Delta k = 0, \quad (2.1.15)$$

the amplitude A_3 of the sum-frequency wave increases linearly with *z*. This special case is known as the condition for perfect phase matching. When the condition (2.1.15) is fulfilled the individual atomic dipoles that constitute the sample are properly phased so that the field emitted by each dipole adds coherently in the forward direction.

When the condition (2.1.15) is not satisfied, the intensity of the emitted radiation is smaller than for the case of $\Delta k = 0$. The amplitude of the sum-frequency field at the exit of the nonlinear medium is given by integrating Eq. (2.1.11) from *z* = 0 to *z* = *L*, being L the length of the crystal,

$$A_3(L) = \frac{2id_{\text{eff}}\omega_3^2}{k_3c^2} A_1 A_2 \int_0^L e^{i\Delta kz}\, dz = \frac{2id_{\text{eff}}\omega_3^2 A_1 A_2}{k_3c^2}\left(\frac{e^{i\Delta kL}-1}{i\Delta k}\right). \quad (2.1.16)$$

The intensity for our definition of field amplitude is given by the time-averaged Poynting vector given by

$$I_i = 2n_i\epsilon_0 c|A_i|^2, \;\; i = 1,2,3. \quad (2.1.17)$$

We thus obtain for our sum-frequency wave an expression that can be written in terms of the incident fields yielding

$$I_3 = \frac{8n_3\epsilon_0 d_{\text{eff}}^2\, \omega_3^4 |A_1|^2|A_2|^2}{k_3c^2}\left|\frac{e^{i\Delta kL}-1}{\Delta k}\right|^2 = \frac{8d_{\text{eff}}^2\, \omega_3^2 I_1 I_2}{n_1n_2n_3\epsilon_0c^2} L^2 \text{sinc}^2\left(\frac{\Delta kL}{2}\right). \quad (2.1.18)$$

The effect of the wavevector mismatch is included entirely in the factor $\text{sinc}^2(\Delta kL/2)$. This is the phase mismatch factor and it is plotted in Figure 2-3. As it can be noted in

Figure 2-3, the efficiency of the three-wave mixing process decreases as $|\Delta k|L$ increases. This happens because if L is greater than approximately 1 / Δk, the output wave can get out of phase with its driving polarization and the power from the ω_3 wave can flow back to the input waves.

In order to achieve an efficient three-wave mixing process, momentum and energy conservation must be fulfilled. Since the linear momentum for photons is given by $\vec{p} = \hbar\vec{k}$, Eq. (2.1.15) represents the conservation of momentum in the photon picture. The energy conservation in nonlinear optical process of SFG is expressed by the relation

$$\omega_3 = \omega_1 + \omega_2. \qquad (2.1.19)$$

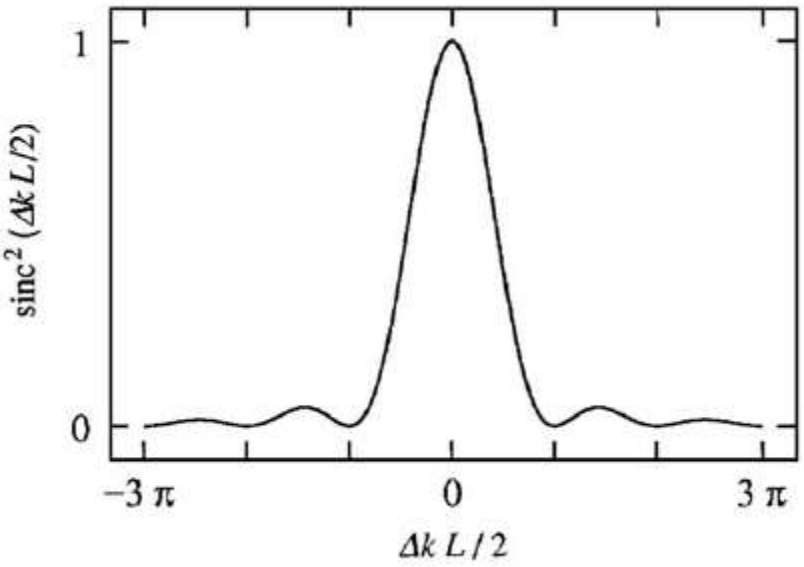

Figure 2-3. Effects of the wavevector mismatch on the efficiency of sum-frequency generation. After (Boyd, 2007).

Experimentally, it is not easy to satisfy Eq. (2.1.15) and Eq. (2.1.19) simultaneously because of the material's normal dispersion where the refractive index is an increasing function of frequency. As a result the condition for perfect phase matching with collinear beams

$$\frac{n_1\omega_1}{c} + \frac{n_2\omega_2}{c} = \frac{n_3\omega_3}{c}, \qquad (2.1.20)$$

where $\omega_3 = \omega_1 + \omega_2$, cannot be achieved. To show this for the case of sum-frequency generation we rewrite Eq. (2.1.26) as

$$n_3 = \frac{n_1\omega_1}{\omega_3} + \frac{n_2\omega_2}{\omega_3}. \qquad (2.1.21)$$

We now express the refractive index difference $n_3 - n_2$as

$$n_3 - n_2 = \frac{n_1\omega_1 + n_2\omega_2 - n_2\omega_3}{\omega_3} = \frac{n_1\omega_1 - n_2\omega_1}{\omega_3} = (n_1 - n_2)\frac{\omega_1}{\omega_3}. \qquad (2.1.22)$$

For normal dispersion, n_3 must be greater than n_2, and hence the left hand of this equation must be positive. However, n_2 must also be greater than n_1, showing that the right hand must be negative, which demonstrates that Eq. (2.1.22) cannot possess a solution.

In principle, it is possible to achieve the phase-matching condition by making use of anomalous dispersion, which occurs in spectral regions with strong absorption that are not desirable in practical devices. To achieve $\Delta k = 0$ anyway, a number of phasematching techniques have been developed (Suhara & Fujimura, 2003). The two most common methods in nonlinear optical devices are the birefringent phasematching (BPM) and quasi-phasematching (QPM). BPM makes use of the birefringence in many nonlinear crystals to satisfy the phasematching condition. QPM is based on a periodic modulation of the nonlinear coefficient d_{eff}. In the next section we will explain the QPM method because it is the method used in this thesis to achieve the phasematching condition.

2.1.4 Quasi-phase-matching

In the previous section we found that the phase-matching condition has to be achieved to get an efficient generation of new frequency components in any nonlinear optical interaction. One of the techniques to achieve this condition is known as quasi-phase-matching (QPM), the idea of QPM is showed in Figure 2-4, which shows a single crystal of nonlinear optical material (a) and a periodically poled material (b). A periodically poled material is a structure that has been fabricated in such a manner that the orientation of one of the crystalline axes, often the *c* axis of a ferroelectric material, is inverted periodically as a function of position within the material. An inversion in the

direction of the *c* axis has the consequence of inverting the sign of the nonlinear coupling coefficient d_{eff}. This periodic alternation of the sign of d_{eff} can compensate for a nonzero wavevector mismatch Δk. It is assumed that the period Λ of the alternation of the crystalline axis has been set equal to twice the coherent buildup length L_{coh} of the nonlinear interaction. Then, each time the field amplitude of the generated wave is about to begin to decrease as a consequence of the wavevector mismatch, a reversal of the sign of *d*eff occurs which allows the field amplitude to continue to grow monotonically. This effect is illustrated in Figure 2-5. Curve (a) shows that for the case of a perfectly matched interaction, the field strength of the generated wave grows linearly with the propagation distance. QPM is illustrated in curve (b). Without phasematching, the refractive indices at the input and at the SFG frequency are not equal. As a consequence, the waves at both frequencies travel through the crystal with different velocities. This is the situation shown in curve (c) where the field amplitude of the generated wave oscillates with propagation distance due to the presence of the wavevector mismatch. Initially, the SFG power increases. But soon, after a certain length called the coherence length L_{coh}, the wavelets have run out of phase and start to cancel out each other via destructive interference. As a consequence, the SFG power decreases again and is zero at z = 2 L_{coh} (Zaske, 2013). An important factor to take into account is that for a constant wavelength satisfying the QPM condition, a shift of the device temperature ΔT gives rise to a phase mismatch that depends on the thermal expansion coefficient of the crystal (Suhara & Fujimura, 2003).

A number of different approaches have been proposed for the fabrication of QPM structures. A particulary promising approach, and the one used in this work, originated with Yamada *et al*. (1993), is the use of a static electric field to invert the orientation of the ferroelectric domains in a thin sample of lithium niobate.

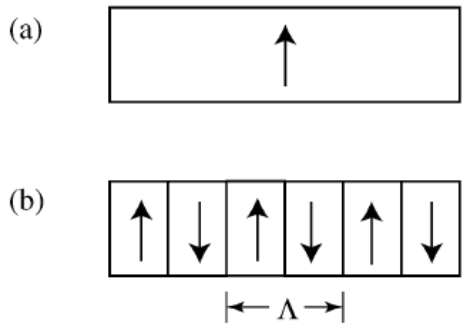

Figure 2-4. Schematic representation of a second-order nonlinear material in the form of (a) a homogeneous single crystal and (b) a periodically poled material in which the positive *c* axis alternates in orientation with period Λ. After (Boyd, 2007).

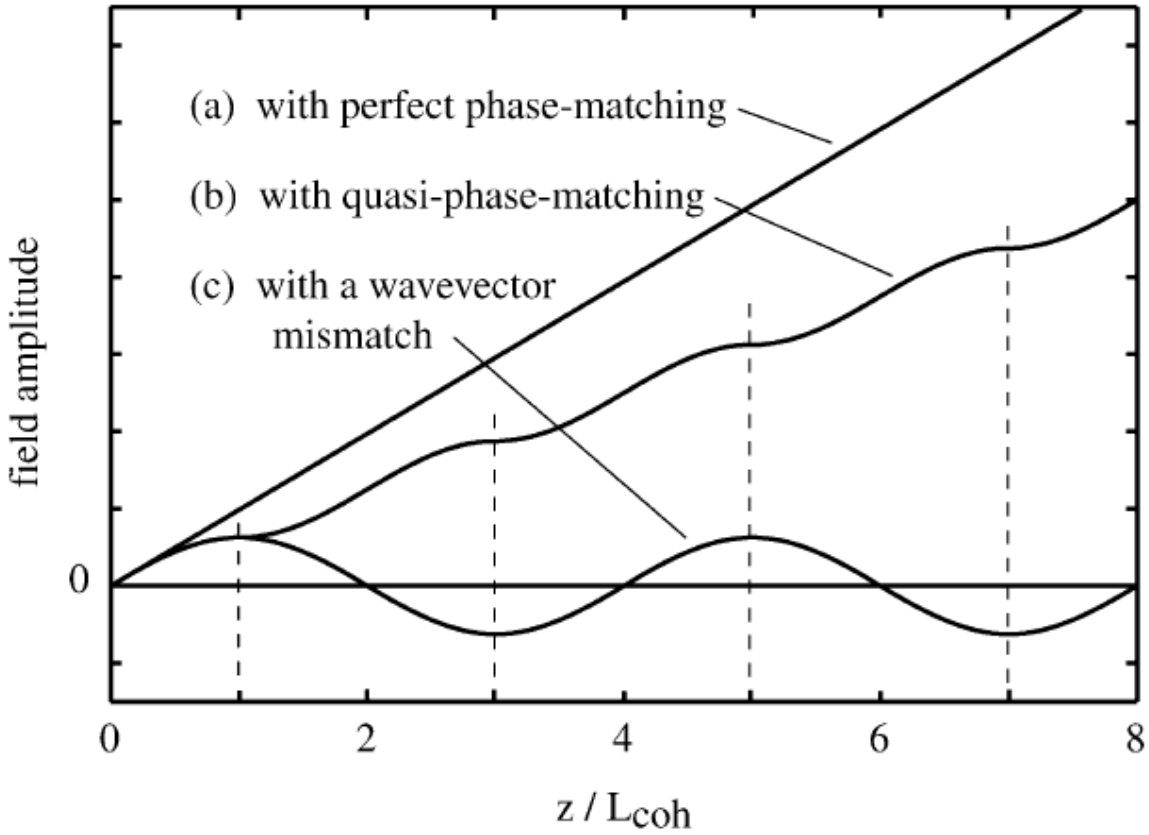

Figure 2-5. Comparison of the spatial variation of the field amplitude of the generated wave in a nonlinear optical interaction for three different phase marching conditions. Curve (a) assumes that the phase-matching condition is perfectly satisfied. Curve (c) assumes that the wavevector mismatch Δ*k* is nonzero, and consequently the field amplitude of the generated wave oscillates periodically with distance. Curve (b) assumes the case of a quasi-phase-matched interaction, in which the orientation of the positive *c* axis is periodically modulated with a period of twice the coherent buildup length L_{coh}, in order to compensate for the influence of wavevector mismatch. In this case the field amplitude grows monotonically with propagation distance, although less rapidly than in the case of a perfectly phase-matched interaction. After (Boyd, 2007).

2.2 Quantum description of light

Most of nonlinear optics experiments are performed with laser light and it is often sufficient to use plane waves to model the electromagnetic fields. But the wave picture of electromagnetic fields is purely classical and cannot explain all of the phenomena we aim to investigate in this work. Because we want to up-convert the frequency of single photons, we have to consider the particle character of light rather than its wave-like properties. For this section we follow the work by Zaske (2013) and Loudon (2000).

2.2.1 Photon number states

The photon number states or Fock states $|n\rangle$ are the basic states of the quantum theory of light. They describe a single mode of the electromagnetic field occupied by *n* photons. To begin we present the Hamiltonian of the quantum mechanical harmonic oscillator in the form

$$\hat{H} = \frac{1}{2}\hbar\omega(\hat{a}\hat{a}^\dagger + \hat{a}^\dagger\hat{a}) = \hbar\omega\left(\hat{a}\hat{a}^\dagger + \frac{1}{2}\right) \tag{2.2.1}$$

where $\hat{a}$ and $\hat{a}^\dagger$ are called the *destruction* and *creation* operators. These operators have the properties

$$\hat{a}|n\rangle = \sqrt{n}|n-1\rangle, \tag{2.2.2}$$

$$\hat{a}^\dagger|n\rangle = \sqrt{n+1}|n+1\rangle, \tag{2.2.3}$$

$$[\hat{a}, \hat{a}^\dagger] = \hat{a}\hat{a}^\dagger - \hat{a}^\dagger\hat{a} = 1. \tag{2.2.4}$$

Taking into account the analogy of the Hamiltonian in Eq. (2.2.1) with the electromagnetic field energy we can apply the formalism of the quantum mechanical harmonic oscillator for light fields. Applying Eq. (2.2.1) to a Fock state we obtain the eigenvalue equation

$$\hat{H}|n\rangle = \hbar\omega\left(\hat{a}\hat{a}^\dagger + \frac{1}{2}\right)|n\rangle = \hbar\omega\left(\hat{n} + \frac{1}{2}\right)|n\rangle = E_n|n\rangle \tag{2.2.5}$$

where the states $|n\rangle$ are simultaneous eigenstates of the Hamiltonian $\hat{H}$ and where we have introduced the *number operator* $\hat{n}$ defined as $\hat{n} = \hat{a}^\dagger\hat{a}$, which has the property

$\hat{n}|n\rangle = n|n\rangle$. From Eq. (2.2.5) we can see that $E_n = \hbar\omega\left(n + \frac{1}{2}\right)$ is the energy of a field mode containing *n* quanta.

2.2.2 Coherent states.

A coherent state, is constructed as a linear superposition of photon number states and it is represented by (Glauber, 1963)

$$|\propto\rangle = e^{-\frac{1}{2}|\alpha|^2} \sum_{n=0}^{\infty} \frac{\alpha^n}{\sqrt{n!}} |n\rangle, \qquad (2.2.6)$$

where *α* is the complex amplitude of the coherent state. The expectation value for the number operator is related to *α* via

$$\langle\hat{n}\rangle = \langle\alpha|\hat{n}|\alpha\rangle = |\alpha|^2. \qquad (2.2.7)$$

The coherent states are important because their properties are the ones that most closely resemble those of a classical electromagnetic wave. A single-mode laser operated well above threshold generates a coherent state excitation.

2.2.3 Different types of light

For the experiments proposed in this work, which lay in the regime of very low optical power and quantum optics, we need single-photon detectors that work differently from normal optical intensity detectors like photodiodes. Single-photon detectors produce a voltage pulse every time a photon event is registered and offer the possibility to investigate the photon statistics in a light beam. Three different classes of light can be distinguished by means of the statistical properties of the intensity fluctuations recorded by single-photon detectors as we can see in Figure 2-6.

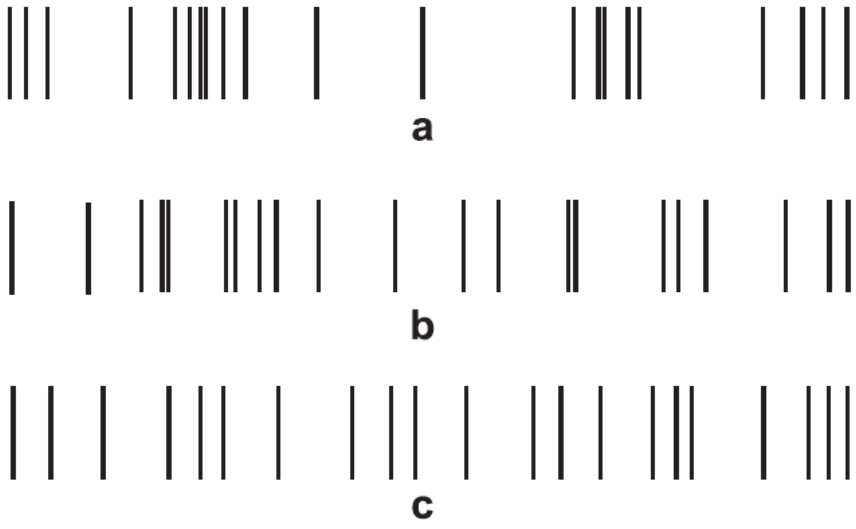

Figure 2-6. Schematic representation of time series of photocounts for light beams that are (a) bunched, (b) random, and (c) antibunched. After (Loudon, 2000).

Figure 2-6(a) shows a schematic representation of the occurrence of photocounts as a function of the time for chaotic light, this light cannot carry a coherent signal and its phase is completely uncertain. The clusters of counts, associated with the photon bunches in the incident light beam, are clearly visible. It can be shown that the photon number probabilities for chaotic light follow the geometric or Planck distribution

$$P(n) = \frac{\langle n \rangle^n}{(1+\langle n \rangle)^{1+n}}, \tag{2.2.8}$$

Illustrated in Figure 2-7 (a). The size of the fluctuation in photon number is characterized by the photon-number variance relation to the mean, defined as

$$(\Delta n)^2 = \langle n \rangle^2 + \langle n \rangle. \tag{2.2.9}$$

Coherent light has no intensity fluctuations in the classical picture and it has no photon bunches in the quantum picture. Figure 2-6(b) shows the random succession of photocounts produced by coherent light. For a coherent state described by Eq. (2.2.6), the probability of finding *n* photons in the mode is governed by the Poisson distribution which is characteristic for random processes as

$$P(n) = |\langle n|\alpha \rangle|^2 = \exp(-|\alpha|^2)\frac{|\alpha|^{2n}}{n!} = e^{-\langle n \rangle}\frac{\langle n \rangle^n}{n!}. \tag{2.2.10}$$

The variance of the Poisson distribution is given by Eq. (2.2.11) and its form is illustrated in Figure 2-7 (b).

$$(\Delta n)^2 = |\alpha|^2 = \langle n \rangle. \qquad (2.2.11)$$

Figure 2-6 (c) shows a succession of photocounts in which the frequency of occurrence of closely-spaced events is less than the frequency of events with larger spacings. A photocount pattern of this form is associated with the so called *antibunched light*. Such light is generated by sources in which emissions of successive photons are more likely to occur with longer time separations than at shorter time intervals.

One can consider a perfectly coherent light source with a Poissonian photon number distribution as a reference for other light sources. Based on this we can classify the different kinds of light intensity fluctutation by means of their root-mean-square deviation of their photon probabilty distribution as it can be seen in Table 2-1.

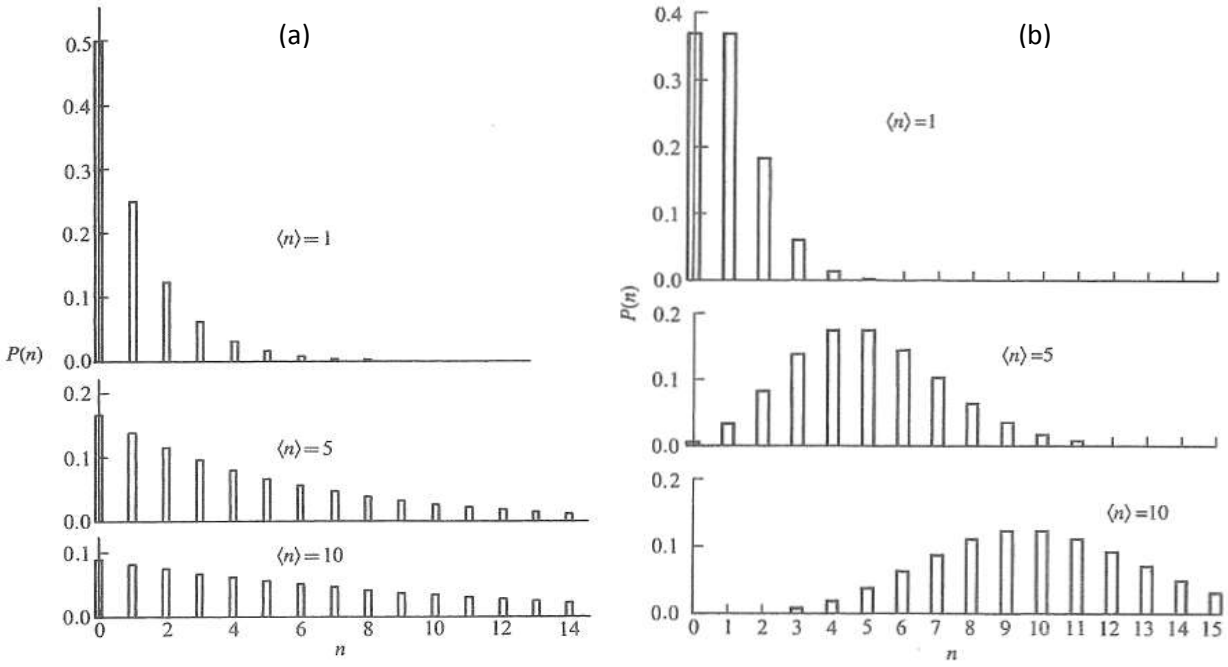

Figure 2-7. The (a) Planck and (b) Poission photon number probability distributions for three different values of photon mean numbers. After (Loudon, 2000).

Table 2-1

Classification of the three classes of intensity fluctuations by means of the root-mean-square deviation of their photon probability distribution.

sub-Poissonian	Poissonian	super-Poissonian
$\Delta n < \sqrt{\langle n \rangle}$	$\Delta n = \sqrt{\langle n \rangle}$	$\Delta n > \sqrt{\langle n \rangle}$

All classical light sources generate super-Poissonian or Poissonian light, and this is why the sub-Poissionan light is also called as non-classical light. An ideal non-classical single-photon source generates photons that are represented by a Fock state which has $\Delta n = 0$. By `ideal' we mean that a single photon can be emitted on-demand with a probability of one at any time specified by the user, the probability for emission of two or more photons at the same time is zero, and photons which are subsequently generated should be indistinguishable. Another desirable feature would be that the repetition rate can be made almost arbitrarily fast. In practice, the ideal case cannot yet be completely achieved due to technical limitations (Lounis & Orrit, 2005).

2.2.4 Degree of second order coherence.

To decide whether a light field is non-classical, poissonian or super-poissonian, we could measure its photon counting statistics but this is very difficult technically because photon counter are not photon number resolvable and have certain death times. Instead, one usually measures the degree of second order coherence. For a stationary light field it is defined by

$$g^{(2)}(\tau) = \frac{\langle \hat{a}^\dagger(t)\hat{a}^\dagger(t+\tau)\hat{a}(t)\hat{a}(t+\tau)\rangle}{\langle \hat{a}^\dagger(t)\hat{a}(t)\rangle^2} \qquad (2.2.12)$$

The classification of light by its photon statistics that we have introduced before can also be written in terms of the value $g^{(2)}(\tau = 0)$, as can be seen in

Table 2-2. In general, light sources that produce states which satisfy $1 - \frac{1}{\langle n \rangle} \leq g^{(2)}(0) < 1$ are called to be nonclassical, the situation $g^{(2)}(0) \geq g^{(2)}(\tau \neq 0)$ is known as photon

bunching, and the situation $g^{(2)}(0) \leq g^{(2)}(\tau \neq 0)$ is known as photon antibunching (Fox, 2006).

This is experimentally measured with the Hanbury-Brown-Twiss (HBT) Interferometer in the quantum picture of light, which is shown in Figure 2-8. (a) Hanbury Brown-Twiss (HBT) experiment with a photon stream incident on the beam splitter. (b) Typical results of such an experiment for bunched light. After .(a) (Hanbury Brown & Twiss, 1956). A stream of photons is incident on a 50:50 beam splitter, and is divided equally between the two output ports. The photons impinge on the detectors and the resulting output pulses are fed into an electronic counter/timer. The counter/timer records the time that elapses between the pulses from D1 and D2, while simultaneously counting the number of pulses at each input. The results are typically presented as a histogram, as shown in Figure 2-8(b). The histogram displays the number of events that are registered at each value of the time τ between the start and stop pulses. Hence the results of the HBT experiment give a direct measure of the second order correlation function in the photon interpretation of light (Fox, 2006).

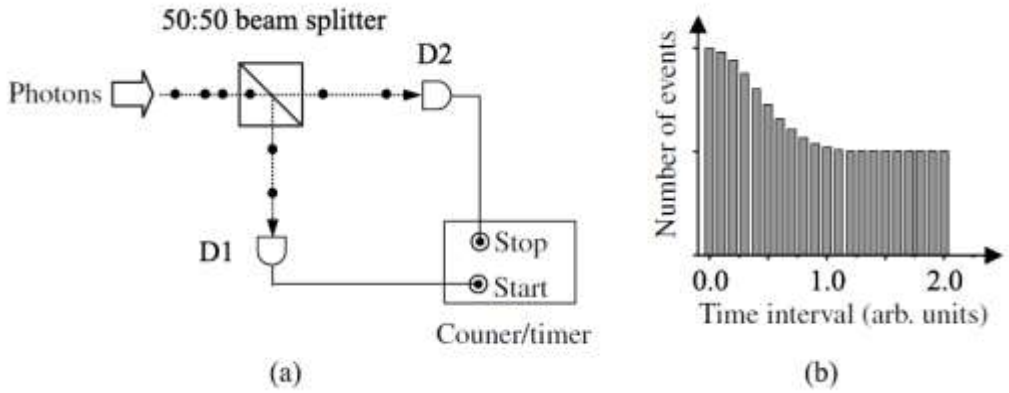

Figure 2-8. (a) Hanbury Brown-Twiss (HBT) experiment with a photon stream incident on the beam splitter. (b) Typical results of such an experiment for bunched light. After (Fox, 2006).

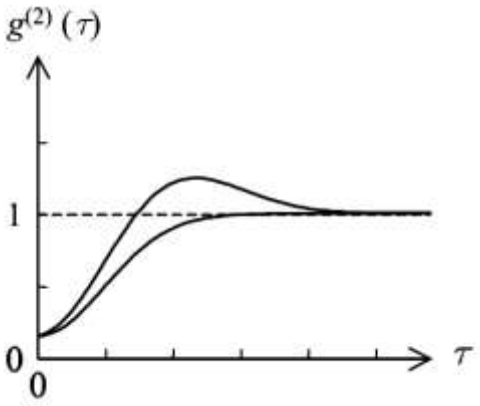

Figure 2-9. Second-order correlation function for two possible forms of antibunched light. After (Fox, 2006).

Table 2-2

Classification of the three classes of intensity fluctuations by means of their degree of second order coherence.		
sub-Poissonian ($\|n\rangle$)	Poissonian ($\|\alpha\rangle$)	super-Poissonian
$g^{(2)}(0)=\frac{\langle n\|\hat{a}^{+}\hat{a}^{+}\hat{a}\hat{a}\|n\rangle}{\langle n\|\hat{a}^{+}\hat{a}\|n\rangle^{2}}=1-\frac{1}{\langle n\rangle}$	$g^{(2)}(0)=g^{(2)}(\tau)=\frac{\langle n\|\hat{a}^{+}\hat{a}^{+}\hat{a}\hat{a}\|n\rangle}{\langle n\|\hat{a}^{+}\hat{a}\|n\rangle^{2}}=1$	$g^{(2)}(0)=1+\frac{(\Delta n)^{2}-\langle n\rangle}{\langle n\rangle^{2}}>1$
$(\Rightarrow 0\le g^{(2)}(0)<1 \quad for \quad n\ge 1)$		

3. Nonlinear Optical Waveguide

In this chapter a description of the nonlinear device used in our experiments is presented. First, the characteristics of the nonlinear material, lithium niobate, as well as its properties for the nonlinear process we are interested in are showed. Then the periodically poled lithium niobate waveguide device is described from a theoretical point of view, ending with its use for SFG.

3.1 Lithium Niobate

Lithium niobate ($LiNbO_3$) is centrally important in integrated and guided-wave optics and one of the most widely used electro-optic materials. It is a human-made dielectric material that does not exist in nature. It was first discovered to be ferroelectric in 1949 (Matthias & Remeika, 1949).

3.1.1 Crystal Structure

Lithium niobate's structure at temperatures below its ferroelectric Curie temperature (around 1210°C) consists of planar sheets of oxygen atoms in a distorted hexagonal close-packed configuration. The octahedral interstices formed in this structure are one third filled by lithium atoms, one-third filled by niobium atoms, and one-third vacant as seen in Figure 3-1. It belongs to the broad class of displacement ferroelectric materials.

The $LiNbO_3$ crystal is a member of the trigonal crystal system. It exhibits three-fold rotation symmetry about its *c* axis and mirror symmetry about three planes that are 60° apart and intersect forming a three-fold rotation axis. These two symmetry operations classify $LiNbO_3$ as a member of the *3m* point group and *R3c* space group. The conventional hexagonal unit cell in $LiNbO_3$ contains six formula weights and the *c* axis is defined as the axis about which the crystal exhibits three-fold rotation symmetry. The coordinate system used to describe the physical tensor properties of lithium niobate is a Cartesian *x, y, z* system. The accepted convention for relating the hexagonal axes to the *x, y, z* principal axes is that the *z* axis is chosen to be parallel to the *c* axis.

3.1.2 Ferroelectricity and Electric Field Poling

The shift of Li^+ and Nb^- ions with respect to the oxygen octahedral at room temperature is the reason for the ferroelectricity in lithium niobate. It causes permanent

electric dipole moments in each unit cell. If all Li^+ ions are shifted in the same direction within a certain volume of the crystal (a domain), the microscopic electric dipoles all point in the same direction and a macroscopic spontaneous polarization $\mathbf{P}_s$ is observed. A periodic modulation of the nonlinear coefficient d_{eff} for QPM in lithium niobate is achieved by periodic poling techniques. This techniques consist on applying external electric fields to a single domain crystal to induce a periodic domain structure with alternating directions (parallel and antiparallel to the initial +*c* direction) of $\mathbf{P}_s$ (Miller, 1998). A domain with a flipped direction of $\mathbf{P}_s$ is equivalent to a mirrored part of the crystal with respect to a fixed frame. Thus, the d_{31} and d_{33} tensor elements change their sign in that region. This is the foundation for the fabrication of QPM crystal via electric field poling (Zaske, 2013).

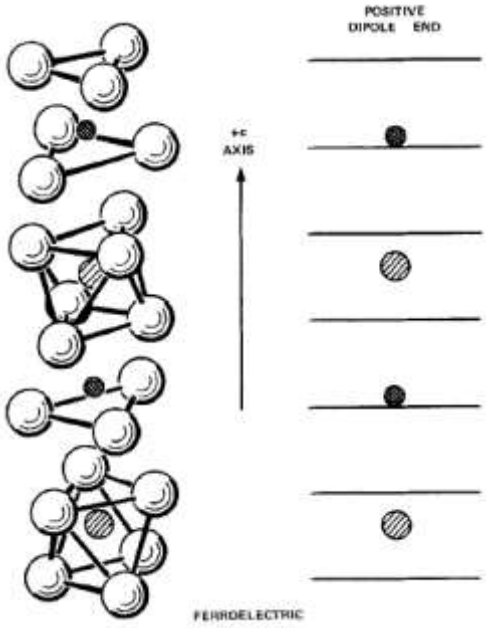

Figure 3-1. Positions of the lithium atoms and niobium atoms with respect to the oxygen octahedra in the ferroelectric phase ($T < T_c$) of lithium niobate, after (Weis & Gaylord, 1985).

3.1.3 Doping

Usually, the composition of lithium niobate single crystals is not perfectly stoichiometric. A small fraction of Li^+ ions is substituted by Nb^- ions such that the ratio of Li^+ ions to Nb^- ions is not exactly 1 as expected from the chemical formula. In the congruent composition of lithium niobate this ratio is 0.946 and this material exhibits and effect

known as photorefractive damage (Ashkin, et al., 1966). This refers to optically-induced inhomogeneities in the refractive index which are observed when the material is illuminated with strong laser radiation in the visible, the complex mechanism for this effect involves several effects. It is associated with the non-perfect stoichiometry of the crystal as Nb^- ions on Li^+ sites can act as traps for electrons which help to form local electric field in the crystal and lead to fluctuations of the refractive index via the linear electro-optic effect (Weis & Gaylord, 1985). The effects produced by the photorefractive damage can be severely detrimental in nonlinear optical processes and can be strongly suppressed by doping the crystal with MgO or ZnO or having a stoichiometric composition (Furukawa, et al., 2000). In this work we work with a congruent lithium niobate crystal doped with ZnO.

3.1.4 Linear and nonlinear optical properties

The transparency range of lithium niobate spans from wavelengths around 0.35μm to 4μm. It is a birefringent material with one optical axis and its birefringence $\Delta n = n_e - n_o$ is negative in the transparency range. In lithium niobate, phase-matching can be achieved by means of the birefringence of the material or by QPM. To know the dependence of the refractive indices on the wavelength and temperature numerous Sellmeier equations can be found in the literature (Jundt, 1997).

Taking into account symmetry properties of the 3*m* point group, the matrix for ***d*** in Section 2.1.1 reads as

$$\boldsymbol{d} = \begin{pmatrix} 0 & 0 & 0 & 0 & d_{31} & -d_{22} \\ -d_{22} & d_{22} & 0 & d_{31} & 0 & 0 \\ d_{31} & d_{31} & d_{33} & 0 & 0 & 0 \end{pmatrix}. \tag{3.1.1}$$

Numeric values for the three non-vanishing tensor elements d_{31}, d_{22}, and d_{33} for congruent lithium niobate can be found in Table 3-1. In this thesis we work with ZnO doped congruent lithium niobate and the doping has no large impact on the values of the nonlinear coefficients. These values are normally obtained from SHG experiments and the d_{33} is the largest and is only accessible via QPM. The light propagation in our experiment is along the *z* axis of the laboratory frame of reference, which is different from the crystal coordinate system as illustrated in Figure 3-2 (Zaske, 2013).

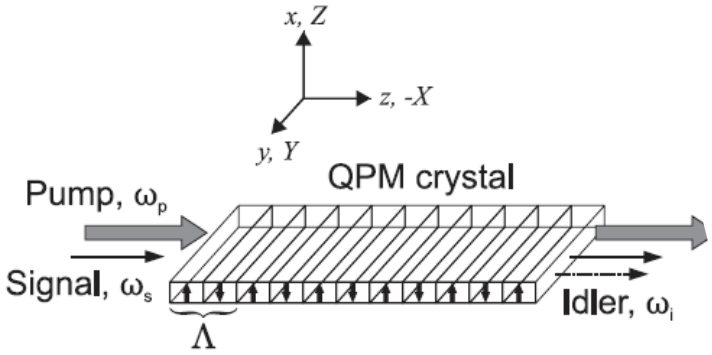

Figure 3-2. Three wave mixing in a QPM crystal. The laboratory frame is denoted by the lower case letters (*x, y, z*) while the capital letters (*X, Y, Z*) indicate the crystal coordinate system of lithium niobate. after (Zaske, 2013).

Table 3-1. Second-order nonlinear-optical coefficients of CLN (pm/V).

Crystal	λ* (μm)	d_{33}	d_{22}	d_{31}	Reference
Congruent $LiNbO_3$ (CLN)	1.313	19.5		3.2	(Shoji, Kondo, Kitamoto, Shirane, & Ito, 1997)
	1.15	25		4.1	(Shoji, Kondo, Kitamoto, Shirane, & Ito, 1997)
	0.852	25.7		4.8	(Shoji, Kondo, Kitamoto, Shirane, & Ito, 1997)
	1.064	27.2	2.1	4.4	(Miller, Nordland, & Bridenbaugh, 1971)

3.2 Waveguide based quasi-phase-matched frequency converter

One way of enhancing the efficiency of nonlinear processes is to use an optical waveguide (WG) to confine light fields within a small spatial volume in two dimensions and to increase the interaction length. For a given power, the intensity increases if the mode volume becomes smaller. We can understand this from the coupled mode equations introduced in Section 2.1.2 and the fact that $|A_m(z)|^2$ is proportional to the field intensities.

The most common examples of optical WGs are the optical fibers made of SiO_2. In this thesis we use WGs made of Zn-doped PPLN with a rectangular cross-section. This material was chosen because of its high nonlinear d_{33} coefficient and its immunity against photorefractive damage, as seen in the previous section. In Figure 3-3 the geometry of a rectangular dielectric waveguide for deriving the theoretical framework in this thesis is shown. The materials on all four sides of the rectangular core are allowed to be different. An exact analytical treatment of this problem is not possible and approximate solutions by numerical methods as accurate as desired have been obtained. Here we follow the treatment from Marcuse (1974) that presents an approximate analytical approach that was developed originally by Marcatili (1969). This method only works for modes far from the cutoff frequency, which is the lowest frequency for which a mode can propagate thorugh the WG. There are two types of modes that the waveguide can support. One type, the E_{pq}^{x} modes, is polarized predominantly in the *x* direction while the other type, E_{pq}^{y}, is polarized predominantly in the *y* direction.

From Marcuse (1974) it is possible to express the transverse field components in terms of the longitudinal components, with the time and *z* dependence ($e^{-i(\omega t-\beta z)}$) we obtain

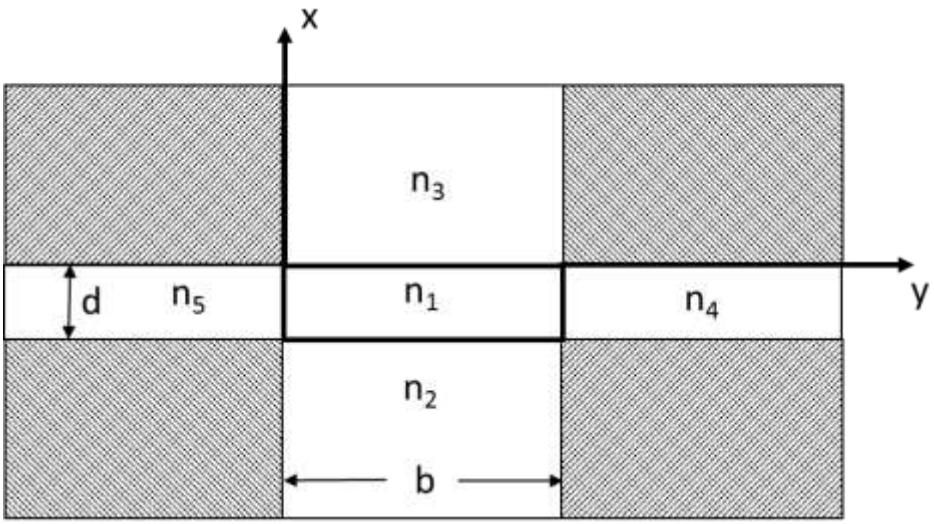

Figure 3-3. Schematic of the five dielectric regions of a rectangular dielectric waveguide. The field in the shaded regions is ignored in the approximation, after (Marcuse, 1974).

$$E_x = -\left(\frac{i}{K_j^2}\right)\left[\left(\beta\frac{\partial E_z}{\partial x}\right) + \left(\omega\mu_0\frac{\partial H_z}{\partial y}\right)\right], \quad (3.2.1)$$

$$E_y = -\left(\frac{i}{K_j^2}\right)\left[\left(\beta\frac{\partial E_z}{\partial y}\right) - \left(\omega\mu_0\frac{\partial H_z}{\partial x}\right)\right], \quad (3.2.2)$$

$$H_x = -\left(\frac{i}{K_j^2}\right)\left[\left(\beta\frac{\partial H_z}{\partial x}\right) - \left(\omega\varepsilon_0 n_j^2\frac{\partial E_z}{\partial y}\right)\right], \quad (3.2.3)$$

$$H_y = -\left(\frac{i}{K_j^2}\right)\left[\left(\beta\frac{\partial H_z}{\partial y}\right) + \left(\omega\varepsilon_0 n_j^2\frac{\partial E_z}{\partial x}\right)\right], \quad (3.2.4)$$

the parameter K_j is defined by $K_j = \left(n_j^2 k^2 - \beta^2\right)^{1/2}$ and n_j $(j = 1, \ldots, 5)$ is the refractive index for each region from 1 – 5. β is the propagation constant, an effective wavenumber for a mode propagating in the WG while $k^2 = \omega^2\mu_0\varepsilon_0 = 2\pi/\lambda$ is the wavenumber in free space. The longitudinal components E_z and H_z must satisfy the reduced wave equation

$$\left(\frac{\partial^2\psi}{\partial x^2}\right) + \left(\frac{\partial^2\psi}{\partial y^2}\right) + K_j^2\psi = 0. \quad (3.2.5)$$

The following set of field component satisfies the reduced wave equation and relations (3.2.1)-(3.2.4) and describes a E_{pq}^x mode in region 1. The time and *z* dependence are omitted for brevity throughout:

$$E_z = A\cos\kappa_x(x+\xi)\cos\kappa_y(y+\eta) \quad (3.2.6)$$

$$H_z = -A\left(\frac{\varepsilon_0}{\mu_0}\right)^{\frac{1}{2}} {n_1}^2\left(\frac{\kappa_y}{\kappa_x}\right)\left(\frac{k}{\beta}\right)\sin\kappa_x(x+\xi)\sin\kappa_y(y+\eta) \quad (3.2.7)$$

$$E_x = \left(\frac{iA}{\kappa_x\beta}\right)(n_1^2k^2 - {\kappa_x}^2)\sin\kappa_x(x+\xi)\cos\kappa_y(y+\eta) \quad (3.2.8)$$

$$E_y = -iA\left(\frac{\kappa_y}{\beta}\right)\cos\kappa_x(x+\xi)\sin\kappa_y(y+\eta) \quad (3.2.9)$$

$$H_x = 0 \quad (3.2.10)$$

$$H_y = iA\left(\frac{\varepsilon_0}{\mu_0}\right)^{\frac{1}{2}} {n_1}^2\left(\frac{k}{\kappa_x}\right)\sin\kappa_x(x+\xi)\cos\kappa_y(y+\eta). \quad (3.2.11)$$

We are interested on E_{pq}^x modes because this are the ones important for the work described in this thesis. To use practically Eqs. (3.2.6)-(3.2.11) and the other sets of functions for regions 1-4, numeric values for κ_x, κ_y, ξ, η, β must be calculated and are completely determined by the refractive indices of the five regions and the height *d* and width *b* of the WG. κ_x and κ_y are found by numerically solving the eigenvalue equations

$$\tan\kappa_x\, d = \frac{n_1^2\kappa_x(n_3^2\gamma_2 + n_2^2\gamma_3)}{n_3^2n_2^2{\kappa_x}^2 - n_1^4\gamma_2\gamma_3} \quad (3.2.12)$$

$$\tan\kappa_y\, b = \frac{\kappa_y(\gamma_4+\gamma_5)}{{\kappa_y}^2-\gamma_4\gamma_5}, \quad (3.2.13)$$

where

$$\gamma_2 = [({n_1}^2 - {n_2}^2)\,k^2 - {\kappa_x}^2]^{\frac{1}{2}} \quad (3.2.14)$$

$$\gamma_3 = [({n_1}^2 - {n_3}^2)\,k^2 - {\kappa_x}^2]^{\frac{1}{2}} \quad (3.2.15)$$

$$\gamma_4 = \left[({n_1}^2 - {n_4}^2)\,k^2 - {\kappa_y}^2\right]^{\frac{1}{2}} \quad (3.2.16)$$

$$\gamma_5 = \left[({n_1}^2 - {n_5}^2)\,k^2 - {\kappa_y}^2\right]^{\frac{1}{2}}. \quad (3.2.17)$$

Once we have κ_x and $\kappa_y$we found $\xi$and η from

$$\tan\kappa_x\,\xi = -({n_3}^2/{n_1}^2)(\kappa_x/\gamma_3) \quad (3.2.18)$$

$$\tan\kappa_y\,\eta = -\gamma_5/\kappa_y. \quad (3.2.19)$$

The propagation constant of a specific mode is obtained from

$$\beta = \left[{n_1}^2 k^2 - \left({\kappa_x}^2 + {\kappa_y}^2\right)\right]^{1/2}. \quad (3.2.20)$$

The power carried by the mode through the WG is obtained by integrating the *z* component of the time averaged power flow vector (Poynting vector):

$$S_z = \mathbf{S} \cdot \mathbf{n} = \frac{1}{2}\mathrm{Re}(\mathbf{E} \times \mathbf{H}^*) \cdot \mathbf{e}_z, \quad (3.2.21)$$

where $\mathbf{n}$ and $\mathbf{e}_z$ are unit vectors, over the infinite transverse cross section of the waveguide

$$P = \iint S_z \, dxdy. \quad (3.2.22)$$

The type of WG used in this work is called Ridge Waveguide and it is shown in Figure 3-4 (a). And Figures 3-4 (b-c) show examples of the intensity distribution in the *xy* plane for the fundamental WG modes.

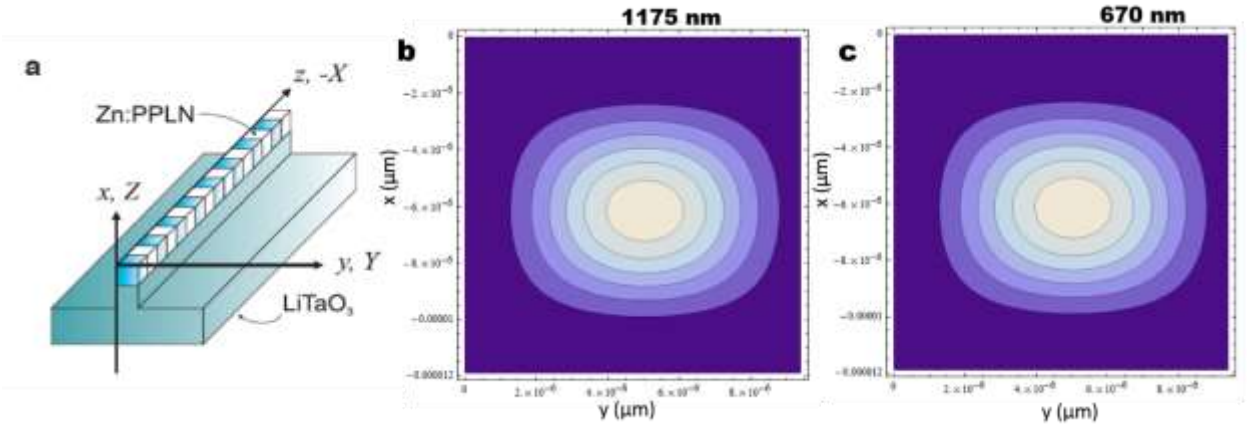

Figure 3-4. (a) Schematic of the Zn:PPLN Ridge Waveguide, after (Zaske, 2013). (b-c) Intensity distribution for the fundamental WG modes for our work's 9.4µm x 11.4µm LN WG. (b) E_{00}^{x} mode for λ = 1175nm, (c) E_{00}^{x} mode for λ = 670nm. Bright areas correspond to high intensity.

3.2.1 SFG in Ridge Waveguides.

This section combines what we saw in Section 2.1 about three-wave mixing due to optical nonlinearities and what we saw in the previous one about field confinement in a WG. Here we describe SFG in lithium niobate ridge WGs. We follow the derivation made by Zaske (2013) and Suhara & Fujimura (2003). First, let us consider three electric field modes

$$\mathbf{E}_m(\mathbf{r},t) = A_m(z)\mathcal{E}_m(x,y)e^{i(\omega_m t-\beta_m z)} + c.c. \quad (m = 1,2,3) \tag{3.2.23}$$

at frequencies ω_1, ω_2 and ω_3 propagating in the WG. The product of the scalar function $A_m(z)$ with the vector field $\mathcal{E}_m(x,y)$ represents the field amplitudes. The evolution of power at ω_m along the WG is described by $A_m(z)$ and only depends on z. The power in Watts is given by $P_m = |A_m(z)|^2$. The normalized transverse intensity distribution is described by $\mathcal{E}_m(x,y)$. $\mathcal{E}_m(x,y)$ is obtained from Marcatili's approximation by multiplication with a normalization factor C_m:

$$\mathcal{E}_m(x,y) = C_m\mathbf{E}_m(x,y), \tag{3.2.24}$$

where

$$C_m = \left[\frac{1}{2}\iint \mathrm{Re}(\mathbf{E}_m \times \mathbf{H}_m^*)\cdot \mathbf{e}_z\, dxdy\right]^{-1/2}. \tag{3.2.25}$$

From Suhara & Fujimura (2003) and with the above definitions, the coupled mode equations governing three-wave mixing processes in WGs are given by

$$\frac{\partial A_1}{\partial z} = -\propto_1 A_1 - i\kappa_1 A_2^* A_3 e^{-i\Delta\beta z}, \tag{3.2.26}$$

$$\frac{\partial A_2}{\partial z} = -\propto_2 A_2 - i\kappa_2 A_1^* A_3 e^{-i\Delta\beta z}, \tag{3.2.27}$$

$$\frac{\partial A_3}{\partial z} = -\propto_3 A_3 - i\kappa_3 A_1 A_2 e^{+i\Delta\beta z}. \tag{3.2.28}$$

Three important changes were made to this equations in comparison to the relations (2.1.17)-(2.1.20) for the interaction of plane waves. The $-\propto_m A_m$ terms were added to account for WG attenuation. The wavevector mismatch Δk was replaced by $\Delta\beta$ because the wave is now propagating in a WG. And the coupling constants κ_1, κ_2, and κ_3 are different from those in (2.1.17)-(2.1.20) and depend on the spatial overlap of the three interacting modes given by the following integrals

$$\kappa_1 = \frac{\omega_1\epsilon_0}{2}\iint \mathcal{E}_1^*(x,y)\, d_Q \mathcal{E}_3(x,y)\mathcal{E}_2^*(x,y)dxdy, \tag{3.2.29}$$

$$\kappa_2 = \frac{\omega_2\epsilon_0}{2}\iint \mathcal{E}_2^*(x,y)\, d_Q \mathcal{E}_3(x,y)\mathcal{E}_1^*(x,y)dxdy, \tag{3.2.30}$$

$$\kappa_3 = \frac{\omega_3 \epsilon_0}{2} \iint \mathcal{E}_3^*(x,y)\, d_Q \mathcal{E}_2(x,y)\mathcal{E}_1(x,y)dxdy. \quad (3.2.31)$$

Where d_Q is the nonlinear coefficient for the *q*-th order of the Fourier series that describes de nonlinear coefficient alternation in a QPM material. These coupling constants obey the next relation, that shows the conservation of total power,

$$\frac{\kappa_1}{\omega_1} = \frac{\kappa_2}{\omega_2} = \frac{\kappa_3^*}{\omega_3}. \quad (3.2.32)$$

For the case of QPM in LN, the integrals (3.2.29)-(3.2.31) are simplified when we assume that only the three fundamental WG modes (*pq* = 00) interact. For this case, Equation (3.2.28) becomes

$$\kappa_1 = \frac{\omega_1 \epsilon_0 d_Q}{2} \iint \mathcal{E}_{1x}^*(x,y)\, d_Q \mathcal{E}_{3x}(x,y)\mathcal{E}_{2x}^*(x,y)dxdy \quad (3.2.33)$$

$$= \frac{\omega_1 \epsilon_0 d_Q}{2} C_1 C_2 C_3 \iint E_{1x}^*(x,y)\, d_Q E_{3x}(x,y)E_{2x}^*(x,y)dxdy, \quad (3.2.34)$$

where (3.2.24) was used for the second equation.

By numerically solving the previous equations Zaske, in his work, set the theoretical basis for QFC and concluded that (Zaske, 2013):

- In the absence of losses, a complete conversion of the telecom field to a visible input field is possible in a LN ridge WG. The required WG length to reach maximum conversion efficiency is on the order of several ten mm if moderate pump powers (100mW order of magnitude) are applied. In this work we refer to conversion efficiency as the total power of converted photons divided by the total input power of signal photons.

4. Frequency up-conversion of laser pulses

In this section we describe the experiments of frequency up-conversion done for this thesis. The main objective is to up-convert single photons at a wavelength of 1180nm emitted from a quantum dot (QD) embedded in photonic crystal (PC) nanocavity to a wavelength of 670nm in the visible range. As described in Section 1.3, the objective can be divided in three stages:

4) Characterization of the periodically poled lithium niobate waveguide (PPLN-WG) nonlinear device in the macro-regime.
5) Demonstrate and characterize the quantum frequency up-conversion of attenuated laser pulses, simulating a single photon source.
6) Demonstrate and characterize the quantum frequency up-conversion of single photons emitted from a QD in a PC nanocavity.

It is worth reminding that, due to the time limitations of a M.Sc. project, the experiments done in this thesis only cover the first stage of the whole project, the characterization of the PPLN-WG.

4.1 Experimental design

4.1.1 Optical Setup

The optical setup for our experiments is shown in Figure 4-1. As our signal laser, a tunable diode laser (*New Focus TLB-6700 Velocity 1165-1185nm*) was used. To guide the 1175 nm signal light to the experiment, its free-space laser output was coupled into a single mode optical fiber by aligning the beam parallel to the optical table with two mirrors (1 & 2, *Newport 10Q20BB.2*) and focusing it into the fiber with an aspheric lens (*Thorlabs C560TME-C, f = 13.86mm*). The pump 1560 nm signal is generated with a tunable laser (*Santec TSL-150, 1535-1565nm*). Its fiber coupled output goes through a fiber polarization controller and then it is feeded into an erbium doped fiber amplifier (*Amonics*) to generate the strong pump field. The 1560 nm pump and 1175 nm signal fields are combined on a dichroic mirror (*Thorlabs DMSP1500*) and coupled into the PPLN WG by an aspheric lens (*Thorlabs C220TME-C, f = 11.00mm*). The details about the PPLN WG are covered in Section 4.1.2. We have to take into

account that the two wavelengths, λ_s and λ_p, have a spectral separation of 375 nm and, because of the chromatic aberration of the lens, the coupling into the PPLN WG with this single aspheric lens is not optimum, see Section 4.2.2. The converted light is collected by an aspheric lens (*Thorlabs A220TM-B, f = 11.00mm*) that collimates it and sends it to a pair of mirrors for alignment. The last stage of the experiment is the filtering and data collection. The filtering is needed because at the output of the PPLN WG there is still some remnant pump and signal fields and we are only interested in the up-converted light. The filtering is achieved by using two prisms (*Thorlabs PS858*) for spatially separating the interest wavelength from unwanted ones. The data is measured with an optical power meter (*Newport 2936-R*) with a silicon detector (*Newport 918D-SL-OD1R*). It is very important to pay special attention to propagation losses in the optical setup. The light coupling from free space propagation into optical fiber and vice versa has to be carefully done to maximize the light transmission. Specifically, coupling light into the PPLN WG requires hyper fine adjustment of the PPLN WG chip position with respect to the input pump and signal fields to assure mode overlapping inside the WG chip and thus, the maximum conversion efficiency. The fine adjustment is achieved with a tens of nanometer resolution x, y, and z position stage (*Thorlabs MAX312D*). In this experiment we achieved a coupling efficiency from Lens 3-PPLN WG-Lens 4 of 40% for the 1550nm pump field and of 95% for the 1175nm signal. Another important loss mechanism is the filtering of the light coming from the PPLN WG chip output. It turns out that the dispersion prisms reflect a considerable amount of light depending on the light polarization so this has to be taken into account. In addition, the polarization from the input fields in the PPLN WG chip has to have the same polarization in order to maximize the conversion efficiency, this is achieved by adjusting the polarization of each input field with the half wave plate (for the signal field) and with the fiber polarization controller (for the pump field).

As seen in Section 1.2.1.4, the PPLN WG chip's temperature has to be precisely controlled to obtain the optimum phase-matching condition. To achieve this, the chip's temperature is set by controlling the current flowing through a thermoelectric cooler (TEC) located in the bottom of the chip housing structure, in direct contact with its metal base. The temperature has to be controlled with a precision of $\pm 0.5°C$ as measured in

4.2, this was achieved with a temperature controller (*Thorlabs TED 200 C*). We used a thermistor (*Thorlabs* TH10K) in direct contact with the chip housing as the temperature sensor.

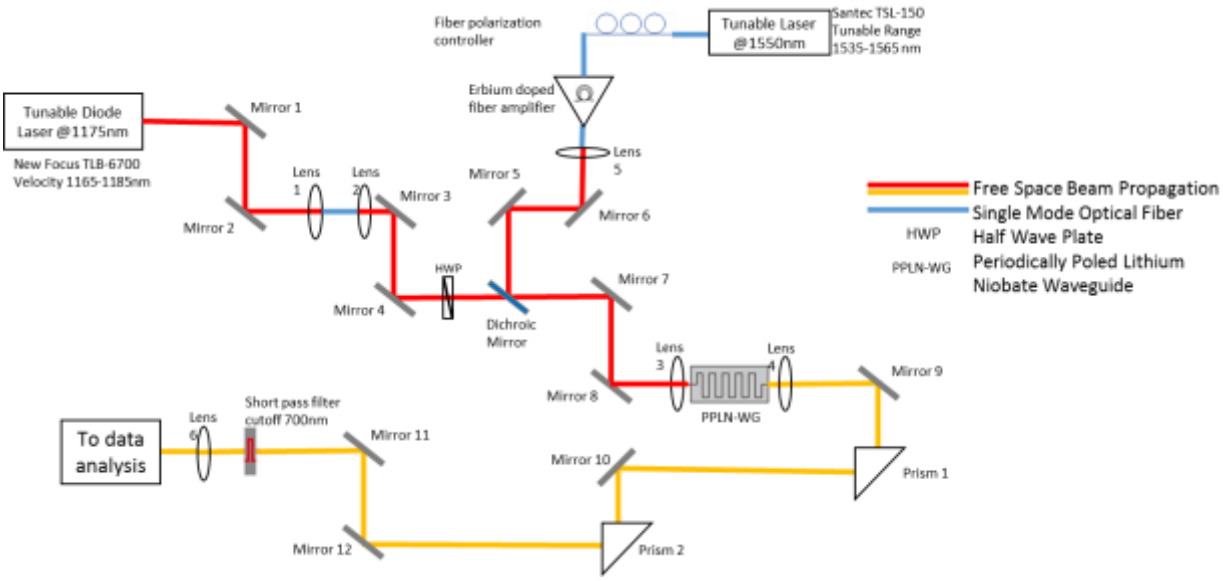

Figure 4-1. Optical setup of the QFC experiment.

4.1.2 PPLN Waveguide Chip

For this up-conversion experiment a PPLN-WG chip (*NTT Electronics,* (NTT Electronics Corp., Japan, 2013)) designed for a SFG wavelength of 670nm (pump: 1175nm, 1558.9nm) is used. The chip consists on twelve ridged weveguides arranged in six groups as shown in Figure 4-2 (A). Each of the groups has a different poling period that allows for different wavelengths tuning by choosing a certain WG, as shown in

Table 4-1. The poling process consists on depositing an array of metallic electrodes with the desired poling period in the surface of the nonlinear crystal. Then, a considerable electric field (in the order of 10^6 V/cm) is applied to change the orientation of the ferroelectric domains under the electrodes. For more details on the fabrication process see (Myers, et al., 1995). The size of the waveguide chip is 40mm long, 4mm wide and 0.5mm thick and picture of it mounted in the translation stage can be seen in Figure 4-3. For this experiment the WG1 of group 2 was used with a phase-matching temperature of 53.5°C.

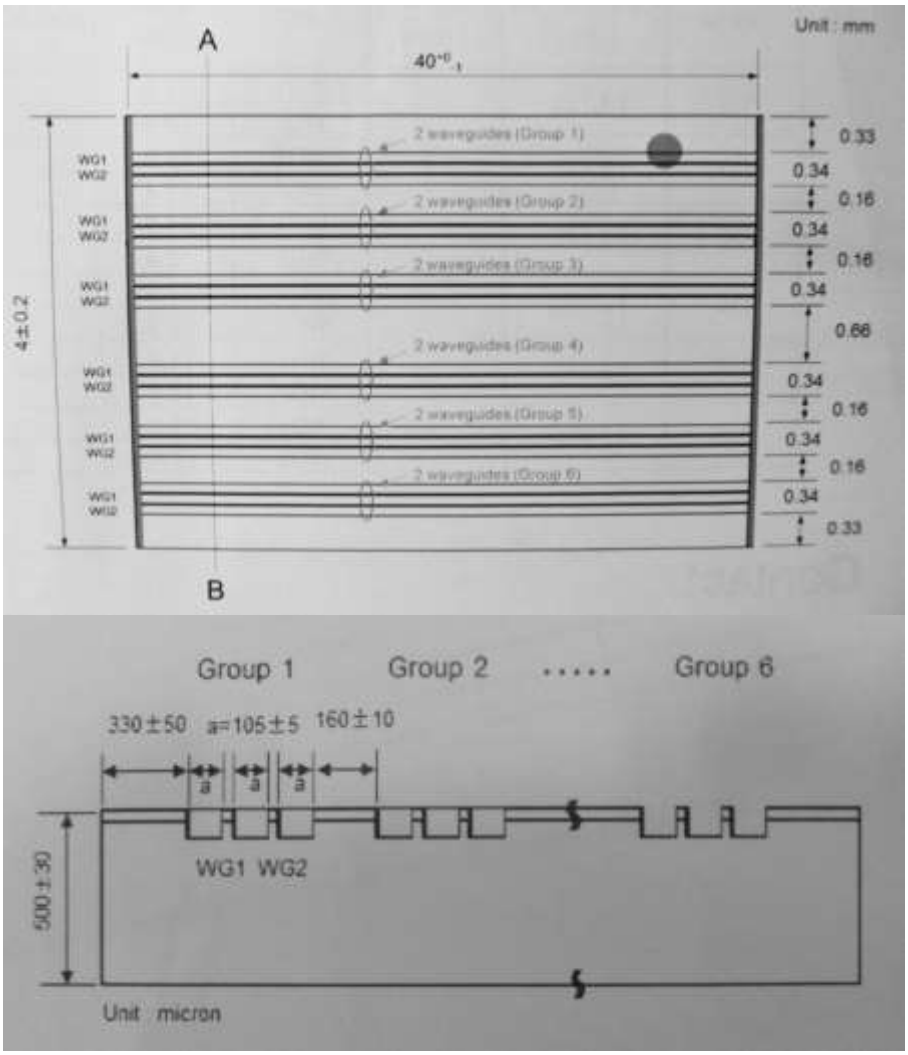

Figure 4-2 Dimensions and layout of the (A) top view and (B) cross-section of the waveguide chip. After (NTT Electronics Corp., Japan, 2013).

4.2 Up-conversion from 1180nm to 670nm. Experimental Results

In this experiments we evaluated the performance of the PPLN WG chip as a frequency converter with macroscopic light power levels (mW). To evaluate the utility of quasi-phase-matched devices for practical applications, it is important to establish tolerances for variations in temperature, wavelength, etc. by evaluating their effects on the efficiency of the device (Fejer, Magel, Jundt, & Byer, 1992). We will describe the performance and conversion efficiency of the converter showing also its phase-matching acceptance and temperature bandwidths. For this section we follow the procedures described in the work by Zaske (2013) and Albota (2006).

Table 4-1. Waveguide data.

Group	Poling period (μm)	Thickness (μm)	WG	Width (μm)	Estimated Phase-matching temperature (°C)
G1	13.125	9.4	WG1	11.9	65
			WG2	12.4	70
G2	13.150		WG1	11.9	54
			WG2	12.4	59
G3	13.175		WG1	11.9	43
			WG2	12.4	47
G4	13.200		WG1	11.9	34
			WG2	12.4	39
G5	13.225		WG1	11.9	24
			WG2	12.4	28
G6	13.250		WG1	11.9	13
			WG2	12.4	17

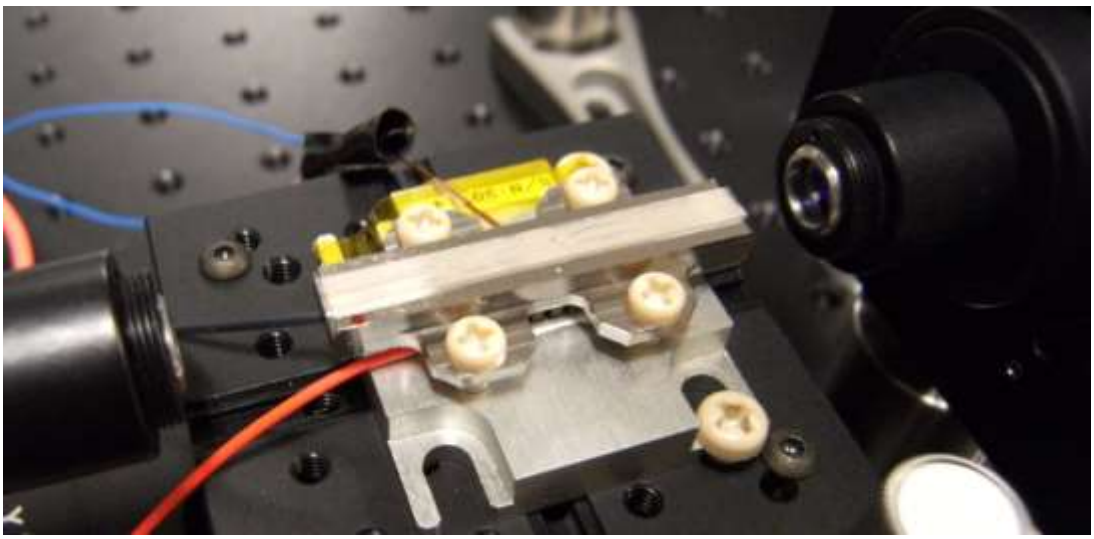

Figure 4-3. Photograph of the PPLN WG chip mounted on the translation stage. The focusing and collecting lenses are also shown.

4.2.1 Performance of the frequency converter

As seen in section 1.2.1.3, for a device of total length L containing uniform periods, the phase-matching factor in the expression for the power conversion efficiency is $\text{sinc}^2(\Delta kL/2)$. We may use the fact that this factor goes to 1/2 when $\Delta kL/2 = 0.4429\pi$ to find the FWHM acceptance bandwidth for several quantities (like the temperature of the crystal, the input wavelengths, the poling period …) which affect Δk when they are varied. Within this acceptance bandwidth the up-conversion process happens efficiently. (Fejer, Magel, Jundt, & Byer, 1992). The signal wavelength acceptance bandwidth $\Delta\lambda_{SFG}$ was experimentally obtained as follows: by fixing the pump wavelength (1558.9 nm) at a 150mW power, we measure the power of the up-converted light with a Si photodetector at the output of the PPLN WG while varying the wavelength of the signal laser in 0.1nm steps around 1170 nm, at a fixed power of 1.2mW. The obtained result is plotted in Figure 4-4 where the data is normalized with respect to the central maximum. By fitting the plot to a sinc^2 function we find that the bandwidth is $\Delta\lambda_{SFG} = 0.39$ nm (FWHM). As we can see, the fit reproduces the data very well around the central maximum but there are notable discrepancies in the tails. These indicate that the phase-mismatch is not constant along the propagation direction because of inhomogeneities of the crystal like imperfect waveguides or temperature variations in the structures (Nash, Boyd, Sargent III, & Bridenbaugh, 1970). We also calculated the theoretical signal acceptance bandwidth for a 40mm crystal with the Sellmeier coefficients from Zelmon, Smaill, & Jundt (1997) that can be compared with the experimental results in Figure 4-5. The theoretical acceptance bandwith is $\Delta\lambda_{TSFG} = 0.28$ nm which is narrower than the experimental result we obtained. In Figure 4-5 we also normalized the measured data area to match the area under the ideal theoretical Sinc^2 curve. With this normalization, the maximum of the measured data is just 0.7 of what theory predicts. This means that the maximum intensity of the converted light that can be expected is less than the ideal theoretical case by a factor of 0.7 (Nash, Boyd, Sargent III, & Bridenbaugh, 1970).

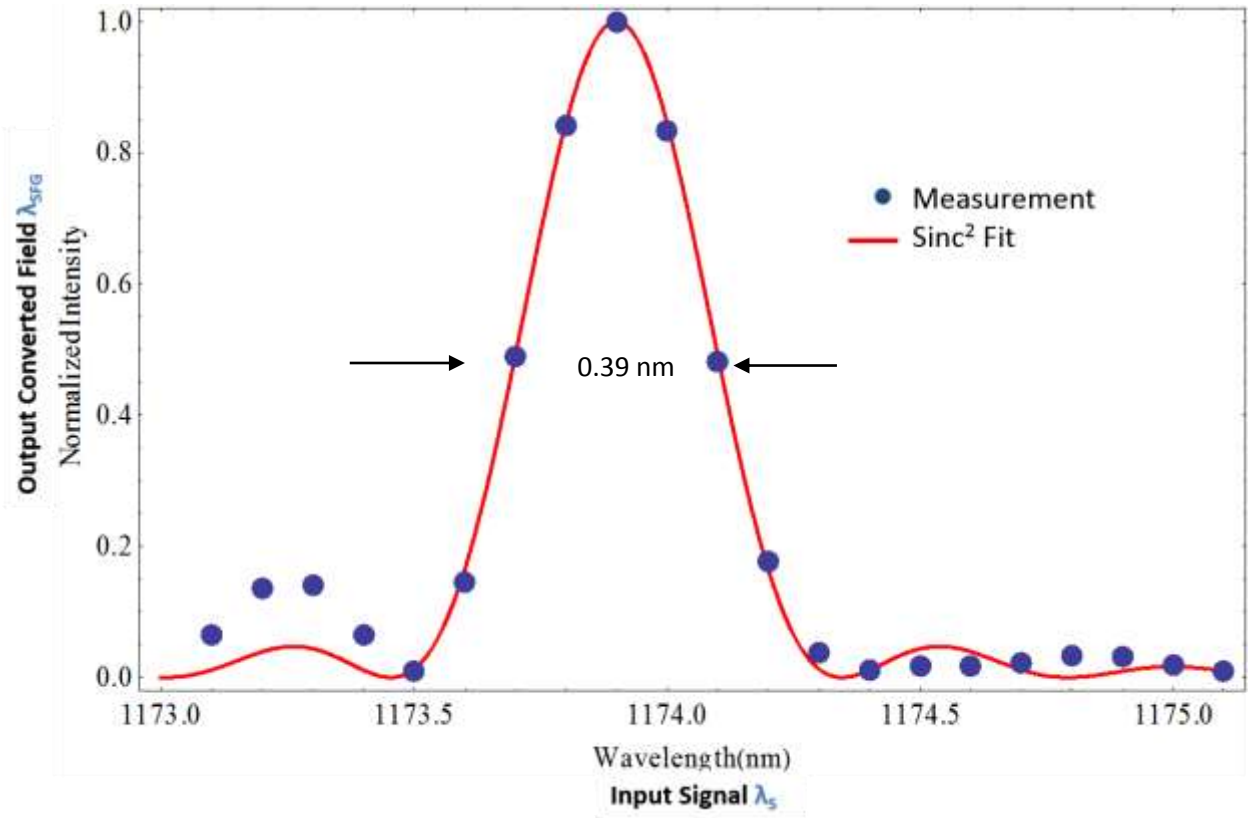

Figure 4-4. SFG acceptance bandwidth for the 40mm long PPLN-WG. The data are normalized with respect to the central maximum.

Similarly, the temperature acceptance bandwidth ΔT_{SFG} was also measured. This was achieved by choosing an operation point of the converter and setting the pump and the signal fields to fixed values, for then to slowly change the temperature of the crystal by means of the external temperature controller. We found a ΔT_{SFG} = 1.06°C from a sinc^2 fit. Figure 4-6 shows the measured curve normalized to its maximum which happens in 53.4°C with λ_P = 1560.775 nm and λ_S = 1174.9 nm. We can see that, as in Figure 4-4, the measured data and the sinc^2 fit match very well in the central lobe, with discrepancies in the function tails. The ΔT_{SFG} = 1.06°C bandwidth is large enough to be accurately controlled by our instrument which has a temperature control resolution of 0.01°C.

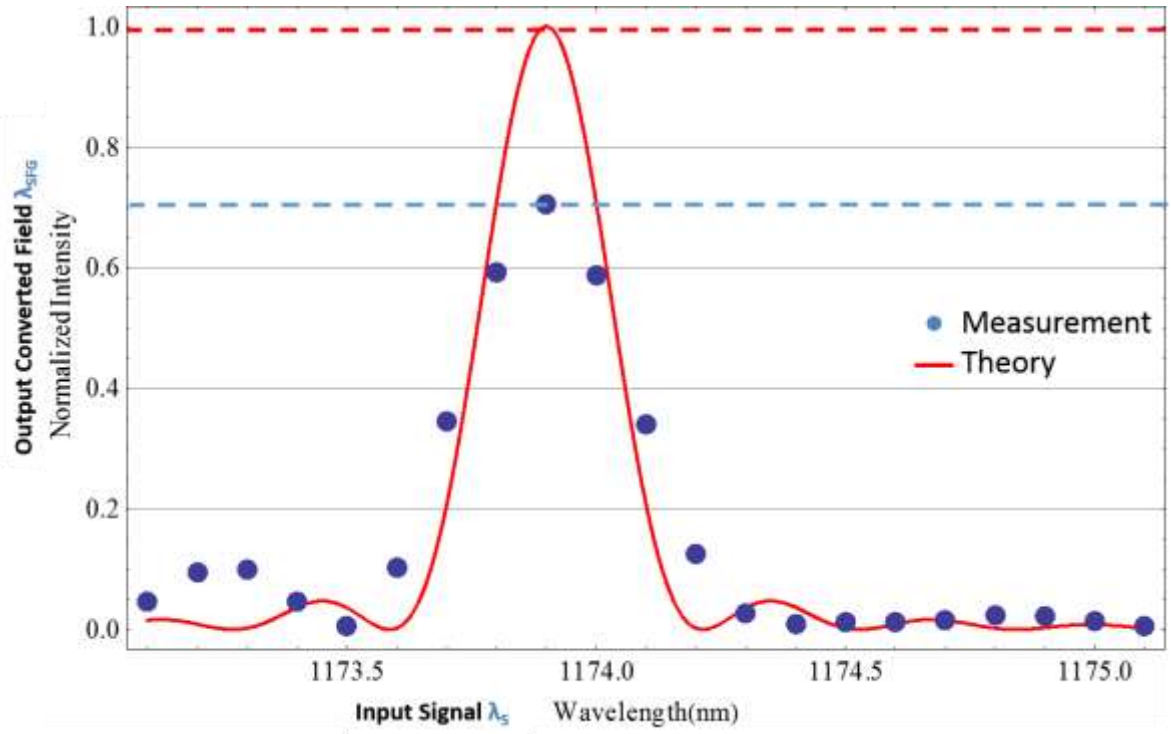

Figure 4-5. Same measured data as in the previous picture but now with different normalization to compare against the theoretical result. The curve is normalized to have the same area as the perfect curve predicted by theory.

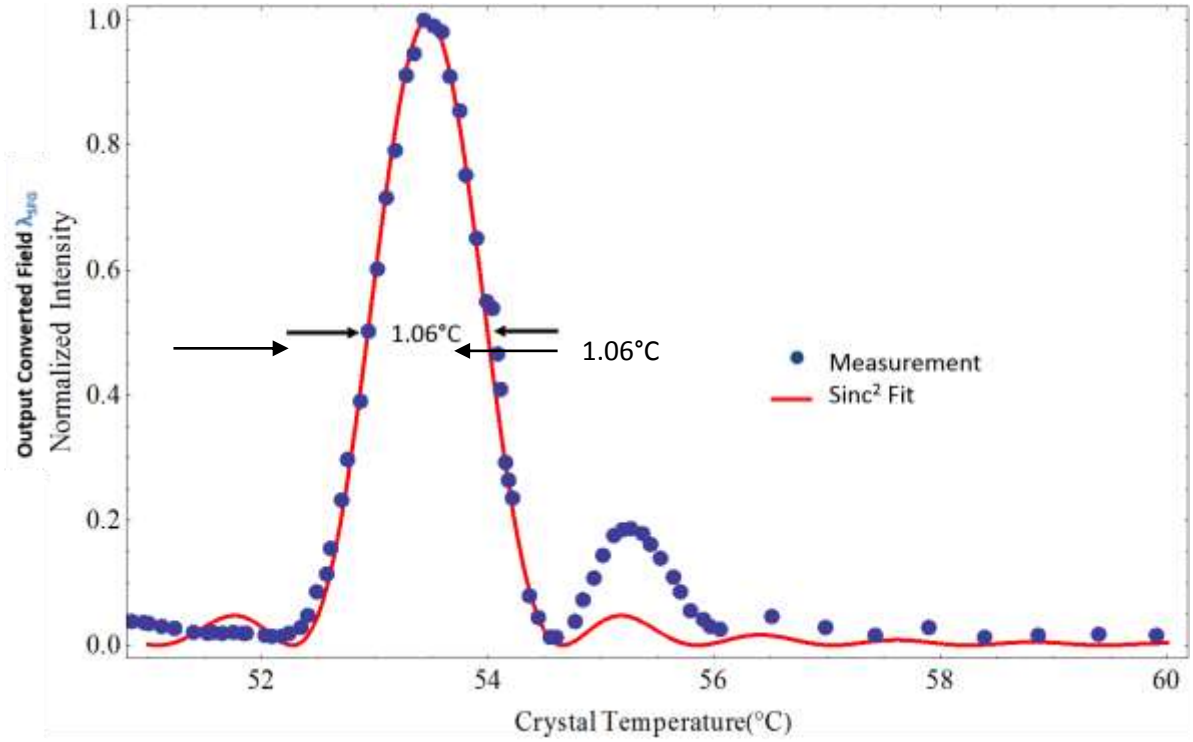

Figure 4-6. Measured temperature acceptance bandwidth and sinc² fit.

We also measured the sum-frequency generation efficiency by means of the input power of the signal and pump fields at the optimum operation point found previously. From the plot shown in Figure 4-7 we can see that the converter reaches a maximum conversion efficiency of around 40% with signal powers greater than 100μW, with an acceptable fixed pump power of 170mW. Now, by fixing the signal field power at 111μW and ramp up the pump power up to 700mw, we achieve conversion efficiencies of almost 70% as shown in Figure 4-8. We have to remember and take into account the not so perfect coupling of both input fields into the waveguide and that for achieving the maximum desired efficiency the optical system has to be as perfectly aligned as possible to assure the minimum losses and the maximum mode overlap in the waveguide.

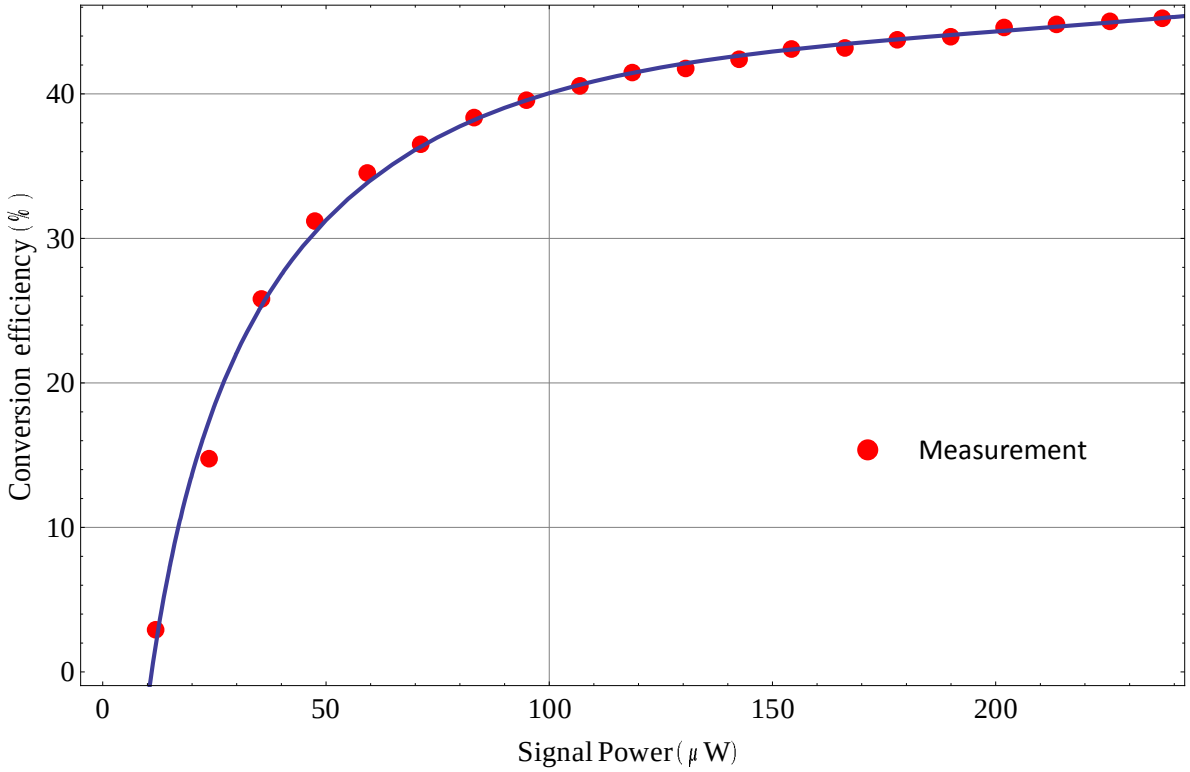

Figure 4-7. Conversion Efficiency varying the signal field power with a fixed pump power of 170mW, λ_P = 1560.775 nm and λ_S = 1174.9 nm.

4.2.2 Summary and discussion

In this chapter we achieved the frequency up-conversion from an 1180nm laser light source to a wavelength of 670nm in the visible. We chose this wavelengths for efficiently detecting the infrared emission of an epitaxial InAs/GaAs quantum dot embedded in a photonic crystal nanocavity with a Silicon APD in the visible, but for the experiments done in this thesis we worked with a laser in the miliwatts regime as a source. First, we introduced the experimental setup for achieving the frequency conversion and described the PPLN WG chip, which is the fundamental device for this experiment. Next, we tested the performance of the setup by obtaining its signal wavelength and temperature acceptance bandwidths. We also measured the converted light power in function of the input light fields and obtained the frequency conversion efficiency of the device. The low coupling efficiency of the 1550nm pump field into the PPLN-WG can be improved by using two lenses in a telescope array as suggested by Zaske (2013). The telescope he proposes consists of two plano-convex lenses, the optimum distance between them can be calculated from the requirement that the two light beams must have the same focus point at the input of the waveguide.

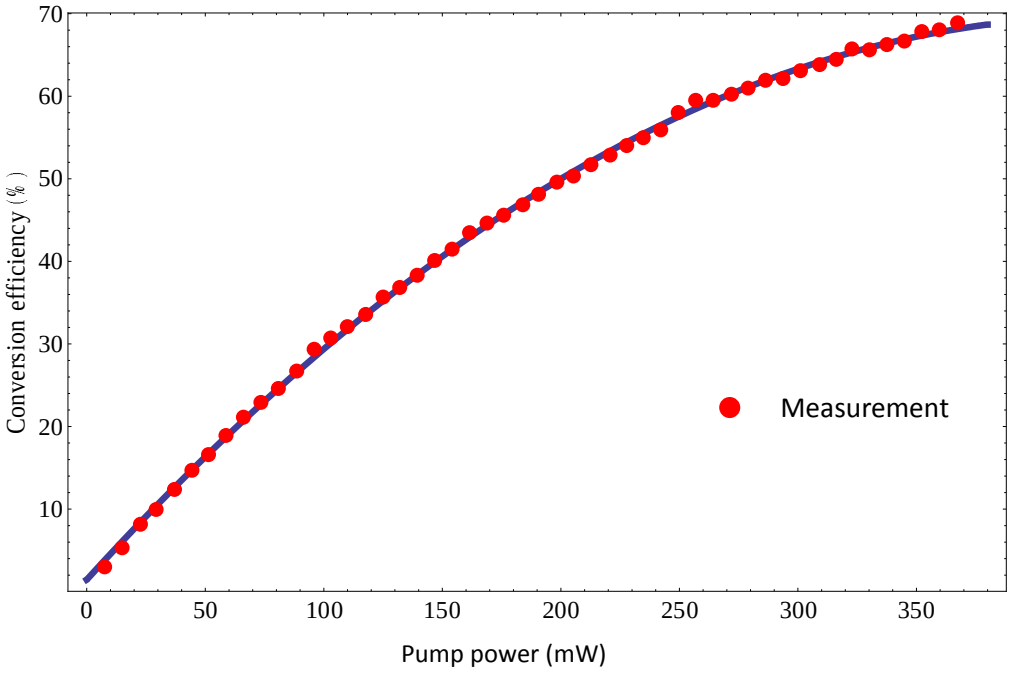

Figure 4-8. Conversion Efficiency varying the pump field power with a fixed signal power of 0.111mW, λ_P = 1560.775 nm and λ_S = 1174.9 nm.

The immediate next stage of this experiment is to emulate a single photon source with attenuated pulses from the signal field laser and study the performance of the device. This can be achieved using a pulse picker and an attenuator in front of our source laser. It is also important to inverstigate the signal to noise ratio (SNR) of the converter, as well as the possible noise sources of the nonlinear processess that take place in the WG and how to overcome them.

5. Summary and Future Prospects

In this work we gave the first step to obtain light fields from the infrared converted to the visible spectral range with the aim to achieve single photon frequency conversion. We mainly studied the performance of the up-conversion process in a PPLN-WG to characterize it and set the basis for experiments in the single photon level. The motivation of this work is to develop an IR-to-visible photonic interface for single photons emitted by semiconductor QDs. Specifically, we want to achieve this quantum frequency up-conversion to characterize the solid state semiconductor single photon sources developed in Dr. Badolato's group, with Silicon single-photon detectors in the visible that perform better than infrared single photon detectors. Moreover we want to overcome spectral distinguishability common to inhomogeneously broadened solid-state quantum emitters by converting spectrally separated QD transition to the same wavelength for its application in future on-chip photonic devices for quantum information processing. After achieving the three stages proposed in Section 1.3 of this work, we will be to efficienctly study the single-photon emission properties of epitaxial InAs/GaAs quantum dots embedded in a photonic crystal nanocavities without the problems that inefficient IR wavelengths detectors imply. This up-conversion interface together with devices that implement the complementary down-conversion process have the potential to connect different elements of future quantum networks.

We achieved frequency up-conversion of light fields from λ_s = 1180nm to λ_c = 670nm in the visible mW range. We measured a maximum process efficiency of 68%, which is quite efficient for this macro-regime. The obtained input signal and temperature acceptance bandwidths of our device give a very good insight of the conditions under it can efficiently work to achieve the maximum conversion of input photons. During the experimental realization of this work we encountered some technical challenges. In section 4.2 we discussed several approaches to overcome this challenges and achieve and even higher conversion efficiency.

This work leads for a future integrated on-chip single photon source with frequency conversion stage that overcomes the source spectral distinguishability for quantum communication applications.

6. Bibliography

Albota, M. A. (2006). *Single-Photon Frequency Upconversion for Long-Distance Quantum Teleportation and Communication.* Ph.D. Thesis, Massachusetts Institute of Technology, Cambridge.

Ashkin, A., Boyd, G. D., Dziedzic, J. M., Smith, R. G., Ballman, A. A., Levinstein, J. J., & Nassau, K. (1966). OPTICALLY-INDUCED REFRACTIVE INDEX INHOMOGENEITIES IN LiNbO3 AND LiTaO3. *Applied Physics Letters, 9*(1), 72-73.

Bennet, C. H., & Brassard, G. (1984). Quantum Cryptography: Public Key Distribution and Coin Tossing. *International Conference on Computers, Systems & Signal Processing* (pp. 175-179). Bangalore, India: IEEE.

Blinov, B. B., Moehring, D. L., Duan, L. M., & Monroe, C. (2004). Observation of entanglement between a single trapped atom and a single photon. *Nature, 428*, 153-157.

Bourennane, M., Gibson, F., Karlsson, A., Hening, A., Jonsson, P., Tsegaye, T., . . . Sundberg, E. (1999). Experiments on long wavelength (1550nm) “plug and play” quantum cryptography systems. *Optics Express, 4*(10), 383-387.

Bourennane, M., Karlsson, A., Pena Ciscar, J., & Mathés, M. (2001). Single-photon counters in the telecom wavelength region of 1550 nm for quantum information processing. *Journal of Modern Optics, 48*(13).

Boyd, R. W. (2007). *Nonlinear Optics* (3rd ed.). Academic Press.

Fejer, M. M., Magel, G. A., Jundt, D. H., & Byer, R. L. (1992, November). Quasi-Phase-Matched Second Harmonic Generation: Tuning and Tolerances. *IEEE Journal of Quantum Electronics, 28*(11), 2631-2654.

Fox, M. (2006). *Quantum Optics An Introduction.* Oxford: Oxford University Press.

Furukawa, Y., Kitamura, K., Takekawa, S., Miyamoto, A., Terao, M., & Suda, N. (2000). Photorefraction in LiNbO3 as a function of [Li]/[Nb] and MgO concentrations. *Applied Physics Letters, 77*, 2494-2496.

Gisin, N., & Thew, R. (2007). Quantum communication. *Nature Photonics, 1*, 165-171.

Glauber, R. J. (1963). Coherent and Incoherent States of the Radiation field. *Phys. Rev.*(131), 2766-2788.

Hanbury Brown, R., & Twiss, R. Q. (1956). Correlation between Photons in two Coherent Beams of Light. *Nature*(177), 27-29.

Hennessy, K., Badolato, A., Winger, M., Gerace, D., Atatüre, M., Gulde, S., . . . Imamoglu, A. (2007). Quantum nature of a strongly coupled single quantum dot-cavity system. *Nature*(445), 896-899.

Jundt, D. H. (1997). Temperature-dependent Sellmeier equation for the index of refraction, ne, in congruent lithium niobate. *Optics Letters, 22*(20), 1553-1555.

Kimble, H. J. (2008). The quantum internet. *Nature, 453*, 1023-1030.

Kumar, P. (1990). Quantum frequency conversion. *Optics Letters, 15*(24), 1476-1478.

Loudon, R. (2000). *The Quantum Theory of Light* (3rd ed.). New York: Oxford University Press.

Lounis, B., & Orrit, M. (2005). Single-photon sources. *Rep. Prog. Phys.*(68), 1129-1179.

Marcatili, E. J. (1969). Dielectric Rectangular Waveguide and Directional Coupler for Integrated Optics. *Bell System Technical Journal, 48*(7), 2071-2102.

Marcuse, D. (1974). *Theory of Dielectric Optical Waveguides.* New York: Academic Press, Inc.

Matthias, B. T., & Remeika, J. P. (1949). Ferroelectricity in the Ilmenite Structure. *Physical Review, 76*(12), 1886-1887.

Miller, G. D. (1998). *Periodically Poled Lithium Niobate: Modeling, Fabrication, and Nonliear-Optical Performance.* Ph.D. thesis, Stanford University.

Miller, R. C., Nordland, W. A., & Bridenbaugh, P. M. (1971). Dependence of Second-Harmonic-Generation Coefficients of LiNbO3 on Melt Composition. *Journal of Applied Physics, 42*(11), 4145-4147.

Myers, L. E., Eckardt, R. C., Fejer, M. M., Byer, R. L., Bosernberg, W. R., & Pierce, J. W. (1995). Quasi-phase-matched optical parametric oscillators in bulk periodically poled LiNbO3. *Journal of the Optical Society of America B, 12*(11), 2102-2116.

Nash, F. R., Boyd, G. D., Sargent III, M., & Bridenbaugh, P. M. (1970). Effect of Optical Inhomogeneities on Phase Matching in Nonlinear Crystals. *Journal of Applied Physics, 41*(6), 2564-2576.

NTT Electronics Corp., Japan. (2013). *Datasheet for the WS-0670-000-A-C-C-TEC PPLN-WG.*

O'Brien, J. L., Furusawa, A., & Vučković, J. (2009). Photonic quantum technologies. *Nature Photonics, 3*(12), 687-695.

Rakher, M. T., Ma, L., Slattery, O., Tang, X., & Srinivasan, K. (2010). Quantum transduction of telecommunications-band single photons from a quantum dot by frequency upconversion. *Nature Photonics, 4*, 786-791.

Raymer, M. G., & Srinivasan, K. (2012). Manipulating the color and shape of single photons. *Physics Today, 65*(11), 32-37.

Resch, K. J., Lindenthal, M., Blauensteiner, B., Böhm, H. R., Fedrizzi, A., Kurtsiefer, C., . . . Zeilinger, A. (2005). Distributing entanglement and single photons through an intra-city, free-space quantum channel. *Optics Express, 13*(1), 202-209.

Roussev, R. V., Langrock, C., Kurz, J. R., & Fejer, M. M. (2004). Periodically poled lithium niobate waveguide sum-frequency generator for efficient single-photon detection at communication wavelengths. *Optics Letters, 29*(13), 1518-1520.

Shapiro, J. H. (2002). Architectures for long-distance quantum teleportation. *New Journal of Physics, 4*, 1-18.

Shoji, I., Kondo, T., Kitamoto, A., Shirane, M., & Ito, R. (1997). Absolute scale of second-order nonlinear-optical coefficients. *Journal of the Optical Society of America B, 14*(9), 2268-2294.

Suhara, T., & Fujimura, M. (2003). *Waveguide Nonlinear-Optic Devices.* Berlin: Springer.

Tanzilli, S., Tittel, W., Halder, M., Alibart, O., Baldi, P., Gisin, N., & Zbinden, H. (2005). A photonic quantum information interface. *Nature, 437*, 116-120.

Tittel, W., & Weihs, G. (2001). Photonic entanglement for fundamental tests and quantum communication. *Quantum Information & Computation, 1*(2), 3-56.

Weis, R. S., & Gaylord, T. K. (1985). Lithium Niobate: Summary of Physical Properties and Crystal Structure. *Applied Physics A, 37*, 191-203.

Wootters, W. K., & Zurek, W. H. (1982). A single quantum cannot be cloned. *Nature, 299*, 802-803.

Zaske, S. (2013). *Quantum Frequency Down-Conversion of Single Photons in Nonlinear Optical Waveguides.* Ph.D. Thesis, Universität des Saarlandes.

Zelmon, D. E., Smaill, D. L., & Jundt, D. (1997, December). Infrared corrected Sellmeier coefficients for congruently grown lithium niobate and 5 mol. % magnesium oxide-doped lithium niobate. *J. Opt. Soc. Am. B, 14*(12), 3319-3322.

Zoller, P., Beth, T., Binosi , D., Blatt, R., Biregel, H., Fabre, C., . . . Zeilinger, A. (2005). Quantum information processing and communication. Strategic report on current status, visions and goals for research in Europe. *The European Physical Journal D, 36*, 203-228.

Acknowledgments

First and above of all I want to thank God and my family because they have been always by my side unconditionally.

Special thanks to Dr. Badolato for all his help during Rochester and support for my future endeavors.

To Yiming Lai, my lab partner at Rochester who taught me everything about this project.

To Dr. Zurita who always pushes us to do our best.

To my friends at INAOE (los rulis de Tona y el M-team), you made this experience unforgettable!

To Conacyt Becas Nacionales and Becas Mixtas program for the funding for my M.Sc. program and research internship.

Last but not least, to Dr. Mondragon who taught us to not ever be conformist.